University of California
Santa Barbara

Elastic Thin Sheets In and Out of Equilibrium

A dissertation submitted in partial satisfaction
of the requirements for the degree

Doctor of Philosophy
in
Physics

by

Zhitao Chen

Committee in charge:

Professor Mark J. Bowick, Co-Chair
Professor M. Cristina Marchetti, Co-Chair
Professor Zvonimir Dogic

March 2024

The Dissertation of Zhitao Chen is approved.

Professor Zvonimir Dogic

Professor M. Cristina Marchetti, Committee Co-Chair

Professor Mark J. Bowick, Committee Co-Chair

March 2024

Elastic Thin Sheets In and Out of Equilibrium

by

Zhitao Chen

Acknowledgements

Graduate school can be quite painful at times, but the people are consistently its redeeming qualities. I am grateful to Mark Bowick for his intellectual and financial support. Mark inspired me to be patient and to keep my head up when I inevitably got stuck in research. His remarkable ability to see and articulate interesting physics in ordinary everyday objects is something I always try to emulate. I would like to thank Cristina Marchetti for her encouragement, which boosted my confidence in physics and beyond, and for being a role model of an exemplary physicist. I appreciate Zvonimir Dogic for serving on my committee, and for his sassy sense of humor which I enjoyed a lot. Many thanks go to my other collaborators: Duanduan Wan, Luiza Angheluta-Bauer, Zhihong You, Supavit Pokawanvit, Amit Samanta, Hong Sun, and Jun Yang. Without them, completing my graduate studies would not have been possible.

Being socially awkward, I do not have a long list of friends and acquaintances to thank that fills pages. I believe, however, that quality is more important than quantity. Thanks to Joe Costello for being a good office mate, a reliable gym buddy, a great friend, and a total inspiration for your contributions to the graduate students' community. Thanks to Amalu Shimamura for being the most supportive friend with whom I feel safe to share thoughts, feelings, gossips, and memes. Thanks to Wayne Weng, the best landlord who saved me a lot of money over the years and helped me come to terms with my inability to distinguish celebrities. Big thanks to Sattivc Ray, the best possible housemate I can ask for. Thanks for the engaging conversations and for your insights into culture. Thanks to Austin Hopkins for the laughter and the meanest turnaround hook shot in basketball. Thanks to Arthur Hernandez for always starting conversations and for being, well, Arthur. Thanks to Aaron Kennon for the maths and the LOLs. Thanks to Seamus O'Hara, Brad Price, and Aleksei Khindanov for fun times during lunches and bonfires.

Thanks to Mathilde Papillon and Molly Kaplan for running inspirations. Thanks to Mark Arildsen for conversations in the office and your encyclopedic knowledge. Thanks to Yaodong Li, Xiaochuan Wu, Farzan Vafa, Paarth Gulati, Toshi Parmar, Roberto Abril Valenzuela, Remi Boros, Nicholas Cuccia, Peter Dotti for the hangouts, parties, and commiseration. Outside of UCSB, thanks to Shangnan Zhou for conversations on sports and life. Thanks to Christopher Jardine for support and conversations on all kinds of topics.

Several others have been tremendously helpful over the past few years. Thanks to Jennifer Farrar for being always on top of things, and for helping me get a TAship in the spring quarter of 2023. Thanks to physical therapists at UCSB Student Health, Andrea Stouffer and Liz Alexander, for helping me work through physical challenges. Huge thanks to my therapists, Karen Dias and Iris Melo, for helping me navigate through emotional challenges and the journey of life.

最后，感谢爸爸陈江谊和妈妈梁淑英，世上最好的父母。

Curriculum Vitæ

Zhitao Chen

Education

2024	Ph.D. in Physics, University of California, Santa Barbara.
2020	M.A. in Physics, University of California, Santa Barbara.
2017	B.S. in Physics and B.A. in Mathematics, Rice University

Publications

1. *Graph-EAM: An interpretable and efficient graph neural network potential framework*, J. Yang*, **Z. Chen***, H. Sun, A. Samanta, J. Chem. Theory Comput. 2023, 19, 17, 5910–5923
2. *Active nematic defects in compressible and incompressible flows*, S. Pokawanvit, **Z. Chen**, Z. You, L. Angheluta, M. C. Marchetti, M. J. Bowick, Phys. Rev. E 106, 054610
3. *Spontaneous tilt of single-clamped thermal elastic sheets*, **Z. Chen***, D. Wan*, M. J. Bowick, Phys. Rev. Lett. 128, 028006 (2022)
4. *The role of fluid flow in the dynamics of active nematic defects*, L. Angheluta, **Z. Chen**, M. C. Marchetti, M. J. Bowick, New J. Phys. 23 033009 (2021)

Preprint

1. *Odd moduli of disordered odd elastic lattices*, **Z. Chen** (arXiv:2204.06587)

* Equal contributions

Abstract

Elastic Thin Sheets In and Out of Equilibrium

by

Zhitao Chen

This thesis investigates two-dimensional theory of elasticity, exploring the effects of thermal fluctuations, non-equilibrium odd elasticity, and disorder.

We use molecular dynamics to study the vibrations of a thermally fluctuating elastic sheet with one end clamped at its zero-temperature length. We uncover a tilted phase in which the sheet fluctuates about an inclined mean configuration, thus breaking reflection symmetry. We determine the phase behavior as a function of the aspect ratio of the sheet and the temperature. We show that tilt may be viewed as a type of transverse buckling instability induced by clamping coupled to thermal fluctuations, and develop an analytic model that predicts the tilted regions of the phase diagram. Unusual responses, as exemplified by the tilted phase, driven by control of purely geometric quantities like the aspect ratio, as opposed to external fields, provide a rich playground for two-dimensional mechanical metamaterials.

We also investigate the impact of disorder on the elastic moduli of an odd elastic material, defined by a non-symmetric elastic tensor. Using an effective medium theory and numerical simulations, we reveal the behavior of effective odd elastic moduli in the presence of disorder, interpreting it as a crossover between the affine response of the passive elastic backbone and a rigidity percolation transition in the odd elastic components. We find that odd elasticity is generally robust against disorder, although certain finely-tuned features may be affected.

Contents

Curriculum Vitae **vi**

Abstract **vii**

1 Introduction **1**
1.1 Statistical Physics of Polymerized Thin Sheets 3
1.2 Overview of Odd Elasticity 11

2 Spontaneous Tilt of Single-Clamped Thermal Elastic Sheets **19**
2.1 Numerical Methods and Characterization 21
2.2 Theoretical Model of Tilt 25

3 Effective Moduli of Disordered Odd Elastic Lattices **31**
3.1 Disordered Odd Elastic Lattices 32
3.2 Overview of Effective Medium Theory 35
3.3 Numerical Simulation Methods 37
3.4 Results 39

A Supplemental Material for Chapter 2 **47**
A.1 Molecular Dynamics Simulations 47
A.2 Finite Element Simulations 51
A.3 Analytical Calculations of In-plane Stress Fields 54
A.4 Effective 1D Theory of Middle Strip 59

B Supplemental Material for Chapter 3 **63**
B.1 Triangular Lattices 63
B.2 Honeycomb Lattices 70

Bibliography **75**

Chapter 1

Introduction

Elasticity, the property whereby a material deforms under the influence of external forces and returns to its original shape and size upon force removal, is a characteristic of most solids. The study of elasticity dates back to ancient human history. Across diverse cultures, ancient engineers demonstrated a practical and intuitive understanding of elasticity through the construction of structurally sound bridges and buildings [1]. A mathematical theory of elasticity, however, was not feasible until the development of Newtonian mechanics. Even then, it took mathematicians and physicists over a century and a half to develop the modern theory of elasticity, characterized by the application of stress and strain tensors, energy functionals, and partial differential equations [2].

The theory of elasticity provides a rigorous framework for analyzing the stability of mechanical structures. Early prominent results include Euler's calculation of critical load [3] and Greenhill's determination of the critical length over which a beam buckles under its own weight [4]. The importance of mechanical stability analysis continues in modern days, influencing the design of diverse structures such as pressure vessels, pipelines, and ship hulls. Recent years have also witnessed an increasing interest in harnessing mechanical instabilities to design mechanical metamaterials with desired properties [5, 6, 7].

This thesis focuses on the elasticity of polymerized or solid thin sheets. We assume that at the continuum level, the stress-strain relation is well defined, and that at the microscopic level, the connectivity among particles is fixed. Notable examples of polymerized thin sheets include biological membranes like the spectrin network in red blood cells [8] and atomically thin two-dimensional materials like graphene and layered transition metal dichalcogenides, which exhibit intriguing mechanical and electronic properties [9, 10]. To describe the mechanical properties of these materials, a two-dimensional theory of elasticity can be formulated, and the theory for thin sheets with large deflections reached its modern form of Föppl-von Kármán theory in the early 20th century. The Föppl-von Kármán theory introduces a set of highly nonlinear partial differential equations, often solved numerically in practical applications. While it might seem that thin sheet theory is reduced to numerical solutions of these equations with suitable boundary conditions, two crucial elements breathe new life into this seemingly mature field.

First, the mechanical behavior of thin sheets is enriched under the influence of thermal fluctuations [11]. As will be reviewed in the following section, thermal fluctuations lead to a low-temperature wrinkled flat phase with anomalous elastic properties in thermalized thin sheets. Analyzing these properties requires insights and techniques from modern statistical physics. In Chapter 2 of this thesis, we focus on the stability and phases of thermally fluctuating thin sheets in a single-clamped configuration.

Second, there is an increasing interest in studying non-equilibrium phenomena in thin sheets and membranes [12]. Traditional elasticity theories are formulated in terms of conservation of energy, which are in general not appropriate for a wide range of living, driven, or active media. A recent example of a non-equilibrium theory of elasticity is known as odd elasticity, in which the stress-strain relation is incompatible with an energy functional [13]. Investigating the robustness of odd elasticity in the presence of disorder is the focus of Chapter 3 of this thesis.

1.1 Statistical Physics of Polymerized Thin Sheets

In this section, we provide an overview of the statistical mechanics of polymerized thin sheets under the influence of thermal fluctuations. We also present fundamental concepts from the theory of elasticity that serve as the foundation for the remainder of this thesis. The presentation below is inspired by the lecture of Nelson from Ref. [9].

To describe a fluctuating thin sheet embedded in a three-dimensional ambient space, we first parameterize its flat undistorted configuration with coordinates $\mathbf{r}_0 = (x_1, x_2, 0)$. For convenience, we will use the notation $\mathbf{x} = (x_1, x_2)$. In general, the thin sheet configuration is given by

$$\mathbf{r}(\mathbf{x}) = \mathbf{r}_0 + \begin{pmatrix} u_1(\mathbf{x}) \\ u_2(\mathbf{x}) \\ h(\mathbf{x}) \end{pmatrix}, \tag{1.1}$$

where u_1 and u_2 describe in-plane displacements, and h describes out-of-plane fluctuations. Here, we use the Monge gauge parameterization and assume the thin sheet to have no overhangs. An undistorted line segment $d\mathbf{r}_0 = (dx_1, dx_2, 0)$ on the sheet is deformed into

$$d\mathbf{r} = \begin{pmatrix} (1 + \partial_1 u_1) dx_1 + \partial_2 u_1 \, dx_2 \\ \partial_1 u_2 \, dx_1 + (1 + \partial_2 u_2) dx_2 \\ \partial_1 h \, dx_1 + \partial_2 h \, dx_2 \end{pmatrix}. \tag{1.2}$$

The stretching of the line segment defines the symmetric strain tensor u_{ij} through

$$d^2 r = d^2 r_0 + 2 u_{ij} dx_i dx_j, \tag{1.3}$$

where, allowing large deflection of the thin sheet, we have

$$u_{ij} = \frac{1}{2} [\partial_i u_j + \partial_j u_i + (\partial_i h)(\partial_j h)]. \tag{1.4}$$

The stretching energy can be expressed as an expansion in powers of u_{ij}, and the total energy is the sum of the bending and stretching energies. For an isotropic thin sheet, the focus of this thesis, the total energy is:

$$E[h, \mathbf{u}] = \frac{1}{2} \int d^2x [\kappa(\nabla^2 h)^2 + 2\mu u_{ij}^2 + \lambda u_{kk}^2], \tag{1.5}$$

where repeated indices are summed over. κ is the bending rigidity (at zero temperature) with dimension of energy, and μ and λ, known as the Lamé parameters, are elastic constants with dimension of energy per area. We truncate the stretching energy at the quadratic order in the strain field u_{ij}. This is known as the Hookean approximation, and gives rise to a linear stress-strain relation (at zero temperature). The Föppl–von Kármán equations can subsequently be derived from this energy functional with variational calculus [14].

To study the statistical physics of thermalized thin sheets, we define the partition function as a path integral:

$$Z = \int Dh D\mathbf{u}\, e^{-E[h,\mathbf{u}]/k_B T}. \tag{1.6}$$

Since the energy functional is quadratic in the in-plane displacement fields, we can integrate them out to obtain an effective energy functional E_{eff} of the height fluctuations alone, which is defined as:

$$Z = \int Dh e^{-E_{eff}[h]/k_B T}, \tag{1.7}$$

where [1]

$$E_{eff}[h] = -k_B T \ln \left(\int D\mathbf{u} e^{-E[h,\mathbf{u}]/k_B T} \right). \tag{1.8}$$

[1]The logarithm in Eq. (1.8) may suggest that E_{eff} is a free energy. The true free energy of the system, however, is given by $F = -k_B T ln Z$. E_{eff} should be interpreted as a Hamiltonian or energy functional of the h field, from which the exact partition function can be calculated through Eq. (1.7).

The effective energy functional reads [15]:

$$\begin{aligned} E_{eff}[h] =& \frac{1}{2}\kappa \int d^2x (\nabla^2 h)^2 + \frac{1}{2} Y \int d^2x [\frac{1}{2} P^T_{ij}(\partial_i h)(\partial_j h)]^2 \\ =& A \sum_{\mathbf{q}} \frac{1}{2}\kappa q^4 h(\mathbf{q}) h(-\mathbf{q}) \\ &+ A \sum_{\substack{\mathbf{q}_1+\mathbf{q}_2=\mathbf{q}\neq 0 \\ \mathbf{q}_3+\mathbf{q}_4=-\mathbf{q}\neq 0}} \frac{Y}{8} [q_{1i} P^T_{ij}(\mathbf{q}) q_{2j}][q_{3i} P^T_{ij}(\mathbf{q}) q_{4j}]\, h(\mathbf{q}_1) h(\mathbf{q}_2) h(\mathbf{q}_3) h(\mathbf{q}_4), \end{aligned} \tag{1.9}$$

where A is the area of the thin sheet, $P^T_{ij}(\mathbf{q}) = \delta_{ij} - q_i q_j / q^2$ the transverse projection operator, and $Y = 4\mu(\mu+\lambda)/(2\mu+\lambda)$ the Young's modulus. The convention for Fourier transform is $h(\mathbf{q}) = \int (d^2x/A) h(\mathbf{x}) e^{-i\mathbf{q}\cdot\mathbf{x}}$.

In the harmonic approximation where we ignore the quartic interaction term, we have the bare height-height correlation function

$$G^0_{hh}(\mathbf{q}) = \langle h(\mathbf{q}) h(-\mathbf{q}) \rangle_0 = \frac{k_B T}{A\kappa q^4}, \tag{1.10}$$

where the subscript 0 denotes a statistical average calculated using only the first term in the effective energy functional. The quartic term is expected to give rise to a renormalized bending rigidity $\kappa_R(q)$ defined by

$$G_{hh}(\mathbf{q}) = \langle h(\mathbf{q}) h(-\mathbf{q}) \rangle \equiv \frac{k_B T}{A\kappa_R(q) q^4}, \tag{1.11}$$

where the expectation value is calculated using the full effective energy functional. A naive application of perturbation theory reveals a length scale l_{th} above which the effect of the quartic term dominates and perturbation theory breaks down [16]. This material-

dependent length scale is known as the thermal length scale, and it is given by

$$l_{th} = \sqrt{\frac{16\pi^3\kappa}{3k_BTY}}. \tag{1.12}$$

Physically, this is the sample size above which the measured bending rigidity $\kappa_R(q)$ of the material differs significantly from its microscopic bending ridigity κ.

Calculations utilizing various methods, including the ϵ-expansion to one loop [17] and higher loop order [18, 19], the self-consistent screening approximation [20], and functional renormalization group [21], reveal that the properties of thermalized thin sheets are controlled by a non-Gaussian (Föppl-von Kármán) fixed point, and the renormalized bending rigidity is given by

$$\frac{\kappa_R(q)}{\kappa} \sim \left(\frac{q}{q_{th}}\right)^{-\eta}, \tag{1.13}$$

for $q < q_{th} = \frac{\pi}{l_{th}}$, with the anomalous exponent $\eta \approx 0.8$. Thermal fluctuations therefore increase the bending rigidity of thin sheets. The Lamé coefficients, and hence the Young's modulus, are also renormalized:

$$\frac{Y_R(q)}{Y} \sim \frac{\mu_R(q)}{\mu} \sim \frac{\lambda_R(q)}{\lambda} \sim \left(\frac{q}{q_{th}}\right)^{\eta_u}, \tag{1.14}$$

with the anomalous exponent $\eta_u \approx 0.4$. In contrast to the bending rigidity, thermal fluctuations soften the in-plane rigidity of thin sheets.

The renormalized bending rigidity and height-height correlation function allow us to calculate a range of mechanical and statistical properties of thermalized thin sheets. A prominent example is the existence of long-range order in the surface normals, indicating that, unlike thermalized one-dimensional polymers which always crumple, thermalized thin sheets exhibit an extended "flat" phase at low temperature [15]. The existence of a symmetry-breaking extended phase does not violate the Mermin-Wagner theorem, which

states that two-dimensional systems with short-ranged interactions cannot spontaneously break a continuous symmetry [22], because the quartic interaction in Eq. (1.9) is in fact long-ranged [23]. In the following, we only review two calculations relevant to the rest of this thesis: the scaling of the root mean square of height fluctuation, and the projected area of thermalized thin sheets.

The mean square height fluctuation is computed as

$$\begin{aligned}\langle h^2\rangle &= \int \frac{d^2x}{A}\,\langle h(\mathbf{x})h(\mathbf{x})\rangle = \sum_{\mathbf{q}}\langle h(\mathbf{q})h(-\mathbf{q})\rangle \\ &= \sum_{\mathbf{q}} \frac{k_BT}{A\kappa_R(q)q^4} \approx \int \frac{d^2q}{(2\pi)^2}\frac{k_BT}{\kappa_R(q)q^4} \\ &\sim \int dq \frac{1}{q^{3-\eta}} \sim L^{2-\eta} \equiv L^{2\zeta},\end{aligned} \tag{1.15}$$

where we have only kept the part of the result divergent with the system size L. The roughness exponent, $\zeta = 1 - \eta/2$ is theoretically predicted to be approximately 0.6. The root mean square of height fluctuation is therefore

$$\frac{h_{rms}}{L} = \frac{\sqrt{\langle h^2\rangle}}{L} \sim L^{-\eta/2}. \tag{1.16}$$

The fact that h_{rms}/L approaches zero in the limit of large system size is a result of the stabilizing effect of the anomalous exponent $\eta > 0$. At low temperature, a thermalized thin sheet is therefore in an extended but rough phase.

The roughness of the extended phase, stemming from thermally induced wrinkles as illustrated in a simulation snapshot in Fig. 1.1, reduces the (projected) area of a thermalized sheet to a value smaller than its area at zero temperature. The area shrinkage

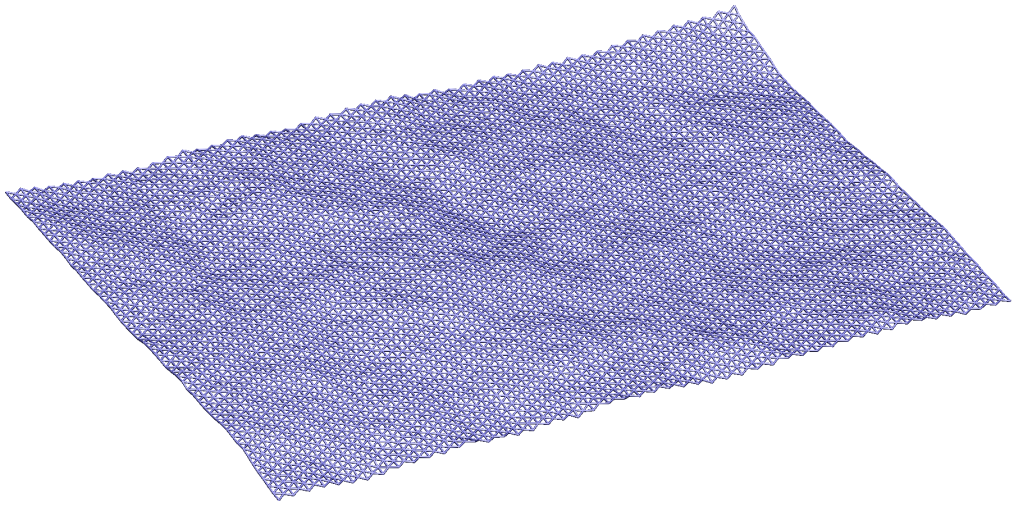

Figure 1.1: Snapshot of a simulation of a freestanding triangulated sheet at $T = 300K$. See Chapter 2 for simulation details.

δA is given by:

$$\frac{\delta A}{A} = \frac{1}{A}\langle \int d^2x\, u_{0,ii}(\mathbf{x})\rangle = \langle u_{0,ii}(\mathbf{q}=\mathbf{0})\rangle \equiv \langle \widetilde{u_{0,ii}}\rangle, \tag{1.17}$$

where $u_{0,ij} = \frac{1}{2}\left(\partial_i u_j + \partial_j u_i\right)$ is the in-plane strain field. The last term is the expectation value of the trace of the Fourier zero mode, which we denote as $\widetilde{u_{0,ii}}$. We present here a general method to compute $(\delta A/A)$ even in the presence of external stress. This was used in Ref. [24] to derive the non-Hookean response to external stress of thermalized sheets, a result previously predicted from a scaling argument in Ref. [25].

To facilitate the calculation, we introduce a source term in the energy functional:

$$\begin{aligned} E_\sigma[h,\mathbf{u}] &= \int d^2x \left\{\frac{1}{2}[\kappa(\nabla^2 h)^2 + 2\mu u_{ij}^2 + \lambda u_{kk}^2] - \sigma_{ij} u_{0,ij}(\mathbf{x})\right\} \\ &= \left\{\frac{1}{2}\int d^2x[\kappa(\nabla^2 h)^2 + 2\mu u_{ij}^2 + \lambda u_{kk}^2]\right\} - A\sigma_{ij}\widetilde{u_{0,ij}}, \end{aligned} \tag{1.18}$$

where σ_{ij} is a spatially uniform tensor, and the last term is outside of the integral. The partition function Z_σ in the presence of the source term is similarly defined as in

Eq. (1.6). Integrating out the in-plane displacement fields, we obtain for the effective energy functional for the height fluctuation in the presence of the source term:

$$E_{\sigma,eff}[h] = \frac{A}{2}\sum_{\mathbf{q}}\big[\kappa q^4 + \sigma_{ij}q_iq_j\big]h(\mathbf{q})h(-\mathbf{q}) + (\text{quartic term}) + (\text{terms quadratic in } \sigma_{ij}), \tag{1.19}$$

where the quartic term is identical to that in Eq. (1.9). Using Eq. (1.18), we obtain

$$\langle\widetilde{u_{0,ij}}\rangle = \frac{1}{Z_\sigma}\int DhD\mathbf{u}\,\widetilde{u_{0,ij}}\,e^{-E_\sigma[h,\mathbf{u}]/k_BT}\Big|_{\sigma_{ij}=0} = \frac{k_BT}{A}\frac{\partial}{\partial\sigma_{ij}}\ln Z_\sigma\Big|_{\sigma_{ij}=0}. \tag{1.20}$$

The last expression can also be computed using the effective energy functional. Omitting the linear in σ_{ij} term, which vanishes after taking the $\sigma_{ij}=0$ limit, we have

$$\begin{aligned}\frac{k_BT}{A}\frac{\partial}{\partial\sigma_{ij}}\ln Z_\sigma\Big|_{\sigma_{ij}=0} =& \frac{1}{Z_\sigma}\int Dh\left(\frac{-1}{2}\right)\sum_{\mathbf{q}}q_iq_jh(\mathbf{q})h(-\mathbf{q})e^{-E_{\sigma,eff}[h]/k_BT}\Big|_{\sigma_{ij}=0}\\ =& -\frac{1}{2}\sum_{\mathbf{q}}q_iq_j\langle h(\mathbf{q})h(-\mathbf{q})\rangle.\end{aligned} \tag{1.21}$$

The area shrinkage is then [24]:

$$\begin{aligned}\frac{\delta A}{A} =& \langle\widetilde{u_{0,ii}}\rangle = -\frac{1}{2}\sum_{\mathbf{q}}q^2\langle h(\mathbf{q})h(-\mathbf{q})\rangle\\ =& -\frac{1}{2}\int\frac{d^2q}{(2\pi)^2}q^2\frac{k_BT}{\kappa_R(q)q^4}\\ \approx& -\frac{1}{2}\Big[\int_{\pi/L}^{q_{th}}\frac{dq}{2\pi}\frac{k_BT}{\kappa(\frac{q}{q_{th}})^{-\eta}q} + \int_{q_{th}}^{\pi/a}\frac{dq}{2\pi}\frac{k_BT}{\kappa q}\Big]\\ =& -\frac{k_BT}{4\pi\kappa}[\eta^{-1} - \eta^{-1}(l_{th}/L)^\eta + \ln(l_{th}/a)],\end{aligned} \tag{1.22}$$

where a is a microscopic cut-off controlled by the average spacing between particles in the system. In the above calculation we have used $\kappa_R(q) \approx \kappa$ for $q > q_{th}$, and $\kappa_R(q) \approx \kappa(q/q_{th})^{-\eta}$ for $q < q_{th}$. The reduction of length along each dimension of the

two-dimensional thin sheet is thus

$$\frac{\delta L_x}{L_x} = \frac{\delta L_y}{L_y} = \frac{1}{2}\frac{\delta A}{A}, \tag{1.23}$$

a result we will utilize in Chapter 2 of this thesis.

While the anomalous elasticity of freestanding thermalized sheets has been explored theoretically for decades, the field has recently advanced considerably on the experimental front with the synthesis of a wide range of two-dimensional materials, such as graphene, hexagonal boron nitride, tungsten disulfide (WS_2), and molybdenum disulfide (MoS_2) [10]. For graphene at room temperature, the thermal length scale l_{th} is approximately a few nanometers. This is a result of both a small bending rigidity $\kappa \approx 1.2eV$ and a large Young's modulus $Y \approx 20\,\mathrm{eV/\AA}^2$ [26, 27, 28]. Experiments conducted with atomically thin freestanding graphene in Ref. [29] revealed a renormalized bending rigidity at room temperature of order 4000 times larger than its microscopic value. It is worth noting, however, that this enhancement is partially due to static ripples from sample preparation, which are predicted to also contribute to the renormalization of the bending rigidity [30]. The predicted softening of the in-plane Young's modulus of a graphene sheet has also been observed experimentally [31]. Such experimental progress has spurred theoretical and numerical efforts to extend the theory of thermalized sheets beyond the pristine, free-standing scenario. This extension is necessary as material samples in experiments often encounter diverse boundary conditions, including supports, clamping, and external stress applied to the samples' boundaries. In Chapter 2 of this thesis, we study a thermally fluctuating sheet with one end clamped at its zero-temperature length. Our study uncovers a tilted phase in which the sheet fluctuates about a mean configuration that is inclined relative to the horizontal plane, thus breaking reflection symmetry. We will show that this tilt may be viewed as a type of transverse buckling instability induced by

clamping in conjunction with thermal fluctuations. Chapter 2 is adapted from a previous publication [32].

1.2 Overview of Odd Elasticity

Conventional theories of elasticity are often built upon (conservative) energy functionals [14]. For example, the statistical and mechanical properties of thermally fluctuating thin sheets reviewed above are derived from the energy functional of Eq. (1.5). This conventional approach, however, may be inadequate for systems driven out of thermal equilibrium. Examples of such non-equilibrium elastic systems arise in the field of active and biological matter, where entities in a system consume free energy to generate forces and motion [33, 34]. Two-dimensional tissues, or epithelia, for instance, exhibit deformations induced by active stresses and torques stemming from cellular processes [35]. To describe the elastic response of these systems, it is necessary to extend the theory of elasticity beyond its traditional framework. Generalizations of the theory of plates and sheets to describe active surfaces are proposed in Ref. [12] and Ref. [36]. For the purpose of this thesis, we focus on odd elasticity, a minimal extension of linear elasticity theory characterized by antisymmetric components of the elasticity tensor [13].

We begin with conventional the two-dimensional theory of elasticity and, for simplicity, focus strictly on in-plane displacements and strain. Dropping height fluctuations from Eq. (1.5), we obtain the energy functional

$$E[\mathbf{u}] = \frac{1}{2}\int d^2x [2\mu u_{ij}^2 + \lambda u_{kk}^2], \tag{1.24}$$

where the strictly in-plane strain is defined as $u_{ij} = \frac{1}{2}(\partial_i u_j + \partial_j u_i) \equiv \frac{1}{2}(u_{j,i} + u_{i,j})$.

Introducing the elasticity tensor

$$C_{ijkl} = \lambda\delta_{ij}\delta_{kl} + \mu(\delta_{ik}\delta_{jl} + \delta_{il}\delta_{jk}), \tag{1.25}$$

we express the energy functional in the following form:

$$E[\mathbf{u}] = \frac{1}{2}\int d^2x\, C_{ijkl}u_{ij}u_{kl}. \tag{1.26}$$

The in-plane stress σ_{ij} is the functional derivative of $E[\mathbf{u}]$ with respect to strain

$$\sigma_{ij}(\mathbf{x}) = \frac{\delta E}{\delta u_{ij}(\mathbf{x})} = C_{ijkl}u_{kl}(\mathbf{x}) = \lambda\delta_{ij}u_{kk}(\mathbf{x}) + 2\mu u_{ij}(\mathbf{x}), \tag{1.27}$$

where the elasticity tensor encodes the linear stress-strain relation. It is convenient to introduce the following basis matrices:

$$\tau^0 = \begin{pmatrix} 1 & 0 \\ 0 & 1 \end{pmatrix} \tag{1.28}$$

$$\tau^1 = \begin{pmatrix} 0 & -1 \\ 1 & 0 \end{pmatrix} \tag{1.29}$$

$$\tau^2 = \begin{pmatrix} 1 & 0 \\ 0 & -1 \end{pmatrix} \tag{1.30}$$

$$\tau^3 = \begin{pmatrix} 0 & 1 \\ 1 & 0 \end{pmatrix}, \tag{1.31}$$

which satisfy the orthogonality condition

$$\tau_{ij}^{\alpha}\tau_{ij}^{\beta} = 2\delta^{\alpha\beta}. \tag{1.32}$$

We can therefore project the stress tensor onto these four basis matrices:

$$\sigma_{ij}(\mathbf{x}) = \tau_{ij}^{0}\sigma^{0}(\mathbf{x}) + \tau_{ij}^{1}\sigma^{1}(\mathbf{x}) + \tau_{ij}^{2}\sigma^{2}(\mathbf{x}) + \tau_{ij}^{3}\sigma^{3}(\mathbf{x}), \tag{1.33}$$

where $\sigma^{\alpha}(\mathbf{x}) = \frac{1}{2}\tau_{ij}^{\alpha}\sigma_{ij}(\mathbf{x})$. We similarly project the *unsymmetrized* strain tensor $u_{i,j}(\mathbf{x})$ on this basis as:

$$u_{i,j}(\mathbf{x}) = \frac{1}{2}\big[\tau_{ij}^{0}u^{0}(\mathbf{x}) + \tau_{ij}^{1}u^{1}(\mathbf{x}) + \tau_{ij}^{2}u^{2}(\mathbf{x}) + \tau_{ij}^{3}u^{3}(\mathbf{x})\big], \tag{1.34}$$

where $u^{\alpha}(\mathbf{x}) = \tau_{ij}^{\alpha}u_{i,j}(\mathbf{x})$. Note that we use a superscript to distinguish the components of the unsymmetrized strain fields $u^{\alpha}(\mathbf{x})$ from the in-plane displacement fields $u_i(\mathbf{x})$. The stress-strain relation in Eq. (1.27) then gives:

$$\sigma^{0}(\mathbf{x}) = \frac{1}{2}\tau_{ij}^{0}\sigma_{ij}(\mathbf{x}) = (\mu+\lambda)\,\tau_{ij}^{0}u_{i,j}(\mathbf{x}) = (\mu+\lambda)\,u^{0}(\mathbf{x}), \tag{1.35}$$

$$\sigma^{1}(\mathbf{x}) = \frac{1}{2}\tau_{ij}^{1}\sigma_{ij}(\mathbf{x}) = 0, \tag{1.36}$$

$$\sigma^{2}(\mathbf{x}) = \frac{1}{2}\tau_{ij}^{2}\sigma_{ij}(\mathbf{x}) = \mu\,\tau_{ij}^{2}u_{i,j}(\mathbf{x}) = \mu\,u^{2}(\mathbf{x}), \tag{1.37}$$

and

$$\sigma^{3}(\mathbf{x}) = \frac{1}{2}\tau_{ij}^{3}\sigma_{ij}(\mathbf{x}) = \mu\,\tau_{ij}^{3}u_{i,j}(\mathbf{x}) = \mu\,u^{3}(\mathbf{x}). \tag{1.38}$$

Expressing the above results in a matrix form, we have:

$$\begin{pmatrix} \sigma^0(\mathbf{x}) \\ \sigma^1(\mathbf{x}) \\ \sigma^2(\mathbf{x}) \\ \sigma^3(\mathbf{x}) \end{pmatrix} = \begin{pmatrix} \mu+\lambda & 0 & 0 & 0 \\ 0 & 0 & 0 & 0 \\ 0 & 0 & \mu & 0 \\ 0 & 0 & 0 & \mu \end{pmatrix} \begin{pmatrix} u^0(\mathbf{x}) \\ u^1(\mathbf{x}) \\ u^2(\mathbf{x}) \\ u^3(\mathbf{x}) \end{pmatrix}. \tag{1.39}$$

To understand the geometry behind Eq. (1.39), we first consider a deformation corresponding to a spatially uniform $u^0(\mathbf{x}) = 2\epsilon$ and $u^\alpha(\mathbf{x}) = 0$ for $\alpha \neq 0$. This deformation can be achieved with displacement fields $u_1(\mathbf{x}) = \epsilon x_1$ and $u_2(\mathbf{x}) = \epsilon x_2$. The effect of this deformation with $\epsilon = 0.2$ on a unit square is depicted in Fig. 1.2(a). Since this deformation expands the unit square isotropically, u^0 corresponds to the mode of dilation, and σ^0 is the pressure [2]. The coefficient $B \equiv \mu + \lambda$ relating pressure to dilation is the bulk modulus. Generally, a spatially uniform $u^\alpha(\mathbf{x}) = 2\epsilon$ can be achieved with displacement fields $u_i(\mathbf{x}) = \tau^\alpha_{ij} x_j$. The effects of all four modes of deformation are illustrated in Fig. 1.2, from which we see that u^1 corresponds to a rotation. Since a local rotation does not change the inter-particle separation, it does not induce any stress in conventional stress-strain materials. σ^1 corresponds to an internal torque density, the antisymmetric part of the stress tensor that gives rise to an extra area integral term when one calculates the total torque on an area element (see section 2 of Ref. [14] for details). From here on, in our discussion of "torque density", it is implied to represent "internal torque density" without the need for explicit mention of "internal". u^2 corresponds to a shear strain along the coordinate axes, and is referred to as shear strain 1 in this thesis. σ^2 is referred to as shear stress 1. Similarly, u^3 corresponds to shear strain along directions diagonal to the coordinate axes, and is referred to as shear strain 2. σ^3 is referred to as shear stress 2.

[2] We adopt the definitions and terminologies in Ref. [37] and the main text of Ref. [13]. Conventionally, however, $\sigma_{ij} = -p\delta_{ij}$ for isotropic compression, and therefore $\sigma^0 = -p$ is negative of pressure.

The Lamé coefficient μ relating shear strains to shear stresses is the shear modulus. That fact the same shear modulus μ relates two independent sets of shear strains and stresses reflects the assumption that the sheet is elastically isotropic.

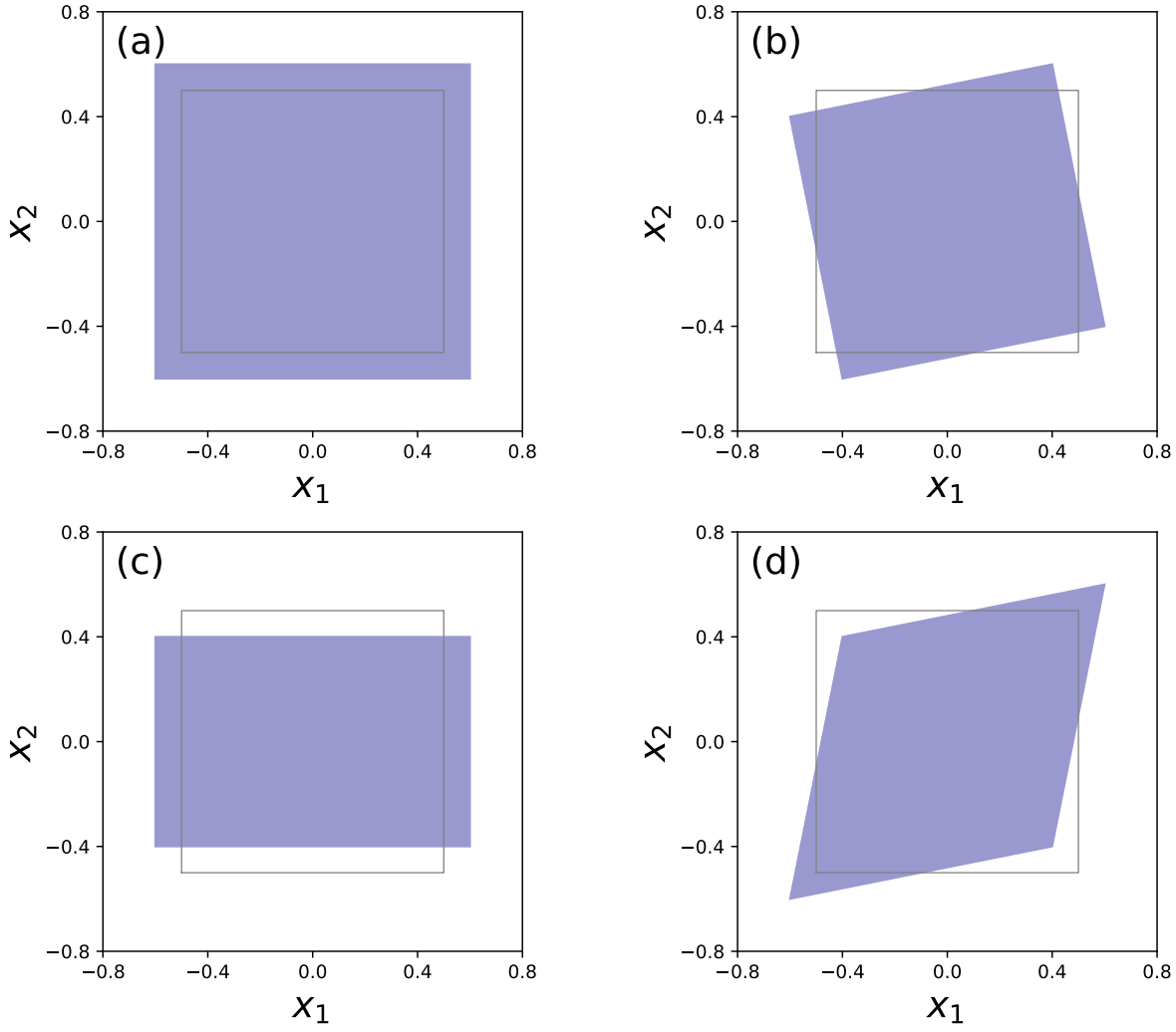

Figure 1.2: Four independent modes of strain in two dimensions. The gray boundaries indicate the undistorted unit squares, and the blue shaded areas represent the distorted squares under (a) dilation, (b) rotation, (c) shear 1, and (d) shear 2.

One can show that Eq. (1.39) is the most general form of linear stress-strain relation in two dimensions, assuming isotropy, conservation of energy (existence of an energy functional), and conservation of angular momentum [13]. In particular, conservation of energy demands the stress-strain matrix to be symmetric [14]. Relaxing the latter two assumptions, isotropic odd elasticity allows additional entries in the stress-strain relation, which takes the following general form:

$$\begin{pmatrix} \sigma^0(\mathbf{x}) \\ \sigma^1(\mathbf{x}) \\ \sigma^2(\mathbf{x}) \\ \sigma^3(\mathbf{x}) \end{pmatrix} = \begin{pmatrix} B & 0 & 0 & 0 \\ A & 0 & 0 & 0 \\ 0 & 0 & \mu & K^o \\ 0 & 0 & -K^o & \mu \end{pmatrix} \begin{pmatrix} u^0(\mathbf{x}) \\ u^1(\mathbf{x}) \\ u^2(\mathbf{x}) \\ u^3(\mathbf{x}) \end{pmatrix}. \tag{1.40}$$

The A modulus couples dilation to torque density, breaking conservation of angular momentum and conservation of energy. The K^o modulus couples the two independent shears in an antisymmetric, non-reciprocal fashion, breaking conservation of energy. The antisymmetric odd moduli give rise to a range of rich behaviors such as net work-extraction under deformation cycles, self-sustained elastic waves even in the over-damped limit, and a negative Poisson ratio. We refer the readers to Refs. [13, 37] for detailed descriptions and derivations.

Until now, our exposition of the theory of elasticity has centered on the continuum limit, where a thin sheet completely fills the space it occupies. It is often convenient, however, to employ microscopic models for elasticity, where a thin sheet is modeled as a collection of discrete interacting particles. Discretized models offer a few advantages. They are well-suited for conducting numerical simulations of thin sheets, and we will use numerical molecular dynamics throughout the remainder of this thesis. They facilitate the introduction of structural inhomogeneity and disorder in the material, a feature we

will utilize in Chapter 3. These models provide a microscopic perspective on mechanical stability, often revealing rich and intricate elastic phenomena [38]. Importantly, for odd elasticity, they offer insight into the microscopic mechanisms that may lead to this unconventional form of elasticity.

Ref. [13] introduced the first microscopic mechanism for odd elasticity through odd springs that exert non-conservative pairwise force on particles. An odd spring with a rest length a connecting particles at $\mathbf{r}_1$ and $\mathbf{r}_2$ exerts a force

$$\mathbf{F} = -\left(k\frac{\Delta\mathbf{r}}{|\Delta\mathbf{r}|} + k^o\frac{\Delta\mathbf{r}^*}{|\Delta\mathbf{r}^*|}\right)(|\Delta\mathbf{r}| - a) \tag{1.41}$$

on the particle at $\mathbf{r}_1$, where k is the passive spring constant and k^o the odd spring constant. $\Delta\mathbf{r} = \mathbf{r}_1 - \mathbf{r}_2$ is the positional separation between the two particles, and $\Delta\mathbf{r}^* = \boldsymbol{\epsilon}\cdot\Delta\mathbf{r}$, where $\boldsymbol{\epsilon}$ is the two-dimensional Levi-Civita tensor. The force exerted by an odd spring is nonconservative because it contains a chiral transverse component represented by the second term in the parenthesis. One can show that the net work done by the system after completing a closed loop of displacement is proportional to the area of the region enclosed by the loop. An odd elastic material can then be assembled with particles connected with odd springs, or with particles that interact with a force law identical to that of an odd spring.

Much like the way conventional elastic moduli can be derived from a microscopic lattice model of interacting particles through a coarse-graining procedure [39], the odd moduli A and K^o can be related to the microscopic odd spring constant k^o [40, 41]. A triangular lattice of particles with nearest-neighbor interactions through odd springs has

odd moduli [3]

$$A = 2K^o = \frac{\sqrt{3}}{2}k^o. \tag{1.42}$$

Since A and K^o are proportional, the violation of energy conservation necessarily implies the violation of angular momentum conservation in an odd elastic triangular lattice. This, however, does not have to be the case in general. Indeed, in a honeycomb lattice where nearest-neighbor particles interact with odd springs with strength k_1^o, and next-nearest-neighbor particles interact with odd springs with strength k_2^o, careful adjustment of the ratio between k_1^o and k_2^o allows for the creation of an odd elastic sheet with $A = 0$ and $K^o = \frac{\sqrt{3}}{2}k_2^o$. Such a material preserves conservation of angular momentum but breaks conservation of energy. In chapter 3 of this thesis, which is adapted from Ref. [42], we explore the effects of disorder on the effective odd moduli of an odd elastic thin sheet. In particular, we show that the fine-tuned conservation of angular momentum in an odd elastic media built from odd springs is not robust in the presence of disorder.

[3] We use the convention that σ_{ij} is the force in the j direction for a surface element in i direction. The external force on a surface with surface normal $\mathbf{n}$ is $\mathbf{F} = \mathbf{n} \cdot \boldsymbol{\sigma}$.

Chapter 2

Spontaneous Tilt of Single-Clamped Thermal Elastic Sheets

The rise of two-dimensional (2D) materials since the synthesis of graphene has created opportunities not only for the fundamental study of elastic sheets in the atomically-thin limit, where their mechanical behavior is enriched by thermal fluctuations, but also for practical applications. Recently, the field has advanced considerably, with the experimental observations in Ref. [29], who studied the deflections and thermal fluctuations of atomically thin, $10\,\mu m$ wide free-standing graphene cantilevers and springs, and found a renormalized bending rigidity at room temperature of order 4000 times larger than its microscopic value at $T = 0$. This remarkable enhancement of the bending rigidity is consistent with the predicted stiffening due to thermal fluctuations alone. The predicted softening of the in-plane Young's modulus [24] of a graphene sheet polymer (by a factor of roughly 25) has also been observed experimentally [31].

While the linear and nonlinear mechanical response of thin sheets, possibly decorated with cuts or holes to facilitate escape into the third dimension [29, 43, 44], is interesting in its own right, one can also envision engineering applications, such as nano-springs,

nanoscale actuators, nano-kirigami and highly sensitive temperature or mass sensors [45]. To compare theoretical predictions with experimental observations, and to properly design mechanical nano-devices at room temperature, one must explore how thermal fluctuations affect the mechanical properties of individual thin sheets, subject to various realistic boundary conditions and geometries [46, 47]. Theoretically, the thermalized behavior of single [48] and double-clamped [49] long ribbons had been studied previously. Ref. [50] demonstrated that in a double-clamped ribbon, the critical buckling strain increases with temperature and is dependent on the system size, and Ref. [51] showed that the critical buckling load also increases with temperature. The buckling transition under the influence of isotropic stress or strain on the boundary [52], as well as external aligning field [53] had been explored with field-theoretical techniques. Inspired by asymmetric coating in realistic thin sheet samples, Ref. [54] uncovered a novel double spiral rolled up phase in inversion-asymmetric thin sheets.

Here we use molecular dynamics (MD) simulations to study a thermal elastic sheet of zero-temperature width W_0 and length L_0, with the aspect ratio $\alpha = (W_0/L_0) \geq 1$, clamped along only one edge of width W_0. We find that besides the horizontal phase where the system vibrates about the horizontal plane, it can also exhibit a tilted phase where the elastic sheet spontaneously tilts, i.e., oscillates about a mean buckled configuration that is tilted with respect to the horizontal plane. Since the tilt plane is equally likely to be above or below the horizontal plane, we have in fact a two-state oscillator. We explore the phase diagram of the system as a function of the temperature and the aspect ratio. Interestingly, the tilted phase only exists for a finite window of the aspect ratio. Further, we provide a theoretical explanation that qualitatively fits the simulation results. As we will show more precisely later, the combination of thermal fluctuations and clamping deforms the reference thin sheet by a length scale proportional to $\frac{k_B T}{\kappa} g(\alpha) L_0$, where g is some function of the aspect ratio. This deformation sets off a competition be-

tween in-plane compression and out of plane bending, and bending is energetically more favorable if the deformation is larger than a length scale approximately proportional to $\frac{\kappa}{YL_0}$. Therefore, we expect a large thin sheet with a small κ and large Y to buckle in our setup at a high temperature, for some aspect ratio. This is consistent with the classic intuition that a long, solid but flexible beam is susceptible to buckling under compression. Apart from clamping, no external forces or fields are present in the setup, so our finding identifies a way of controlling the states of 2D materials by pure geometry and temperature.

2.1 Numerical Methods and Characterization

We model an elastic sheet as a discrete triangular lattice of vertices and bonds, with the elastic energy being a sum of a stretching term and a bending term:

$$E = \frac{\varepsilon}{2} \sum_{\langle ij \rangle} \left(|\mathbf{r}_i - \mathbf{r}_j| - a \right)^2 + \frac{\tilde{\kappa}}{2} \sum_{\langle IJ \rangle} \left(\hat{\mathbf{n}}_I - \hat{\mathbf{n}}_J \right)^2 , \tag{2.1}$$

where ε is the discrete spring constant, a is the equilibrium spring length and $\tilde{\kappa}$ is the discrete bending modulus. The sum $\langle ij \rangle$ is over pairs of nearest-neighbor vertices, with positions $\mathbf{r}_i$ in 3D Euclidean space, while the sum $\langle IJ \rangle$ is over all pairs of triangular plaquettes, with unit normals $\hat{\mathbf{n}}_I$, that share a common edge. The continuum limit of Eq. (2.1) leads to a Young's modulus $Y = 2\varepsilon/\sqrt{3}$, a bending rigidity $\kappa = \sqrt{3}\tilde{\kappa}/2$ and a Poisson ratio $\nu = 1/3$ [55, 56, 57]. For graphene the discrete triangular lattice may be viewed as the dual of its actual honeycomb lattice [49] with edge length $a = \sqrt{3}a_0$, where $a_0 = 1.42\text{Å}$ is the carbon-carbon bond length. We use graphene's microscopic material parameters $\kappa = 1.2\,\text{eV}$ [58, 26] and $Y = 20\,\text{eV/Å}^2$ [27, 28]. Fig. 2.1(a) displays the zero-temperature flat configuration of a sheet in the $x - y$ plane, with $L_0 = 20a \approx$

50Å and aspect ratio $\alpha = W_0/L_0 \approx 5$, where the subscript 0 labels zero-temperature quantities. We clamp the edge vertices along one zigzag boundary indicated by the pink line in Fig. 2.1(a) and tag the middle vertex on the free end (shown in red). We find consistent results from MD simulations using two different software packages: HOOMD-blue [59, 60] and LAMMPS [61]. After giving the free vertices a small random out-of-plane displacement, we update their positions with the Nosé-Hoover thermostat, in which the the system reaches a target temperature and evolves in the constant temperature (NVT) ensemble (see Appendix A for details). Every simulation run consists of 10^7 time steps in total, with the first 5×10^6 time steps ensuring equilibrium.

Our system exhibits two phases depending on the aspect ratio and the temperature: a horizontal phase where the sheet vibrates about the horizontal $z = 0$ plane, and a tilted phase where it vibrates about a tilted configuration. We show snapshots of the two phases in Figs. 2.1(b) and (c). It is revealing to plot the height h (z coordinate) of the middle vertex of the free long edge (the red vertex in Fig. 2.1(a)) for 10^6 timesteps after equilibrating – see Fig. 2.1(d). At low temperature ($kT = 0.1$eV), the red vertex vibrates about $z = 0$ (black line). At a higher temperature ($kT = 0.8$eV), however, the vertex vibrates about $z \approx 10$ – the upper trace (blue line). At an intermediate temperature ($kT = 0.5$eV), the vertex vibrates about two symmetric positions $z \approx \pm 7$ with occasional inversions (red line).

We quantify tilt with an order parameter $\phi \equiv \langle |h/x| \rangle$, where h and x are coordinates of the aforementioned vertex, and the bracket denotes an average over time and independent runs. We plot ϕ as a function of aspect ratio α and temperature kT in Fig. 2.2, where we have averaged over five independent runs. At sufficiently high temperature and in a moderate range of aspect ratios, the sheet is clearly tilted; otherwise the sheet is horizontal. We do not observe any abrupt discontinuity in Fig. 2.2, which suggests that the transition between the horizontal phase and the tilted phase is continuous. For a

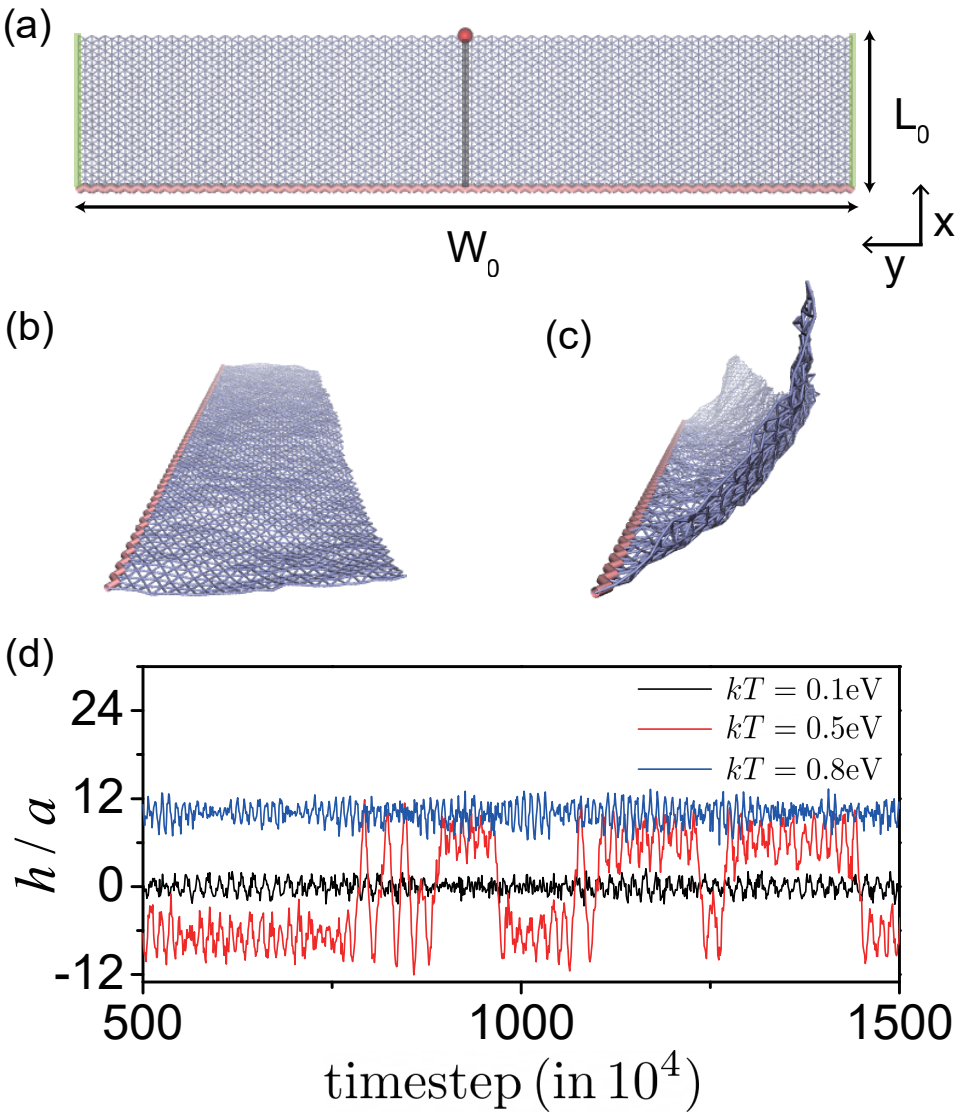

Figure 2.1: (a) A triangulated membrane with zero-temperature length $L_0 = 20a$ and aspect ratio $\alpha = W_0/L_0 \approx 5$ clamped on the back edge (colored pink). The middle vertex on the front edge is marked with a large red dot. We label the left and right edges in green, and the centerline in grey. The snapshot was generated using the Visual Molecular Dynamics (VMD) package [62] and rendered using the Tachyon ray tracer [63]. (b) Snapshot of the horizontal phase. (c) Snapshot of the tilted phase. (d) Height (measured in the zero-temperature lattice spacing a) of the red vertex as a function of time for 10^6 time steps after equilibrating for 5×10^6 time steps.

system with an aspect ratio in the window for tilt the free energy gradually changes from having only one global minimum (horizontal phase) to having two equal local minima

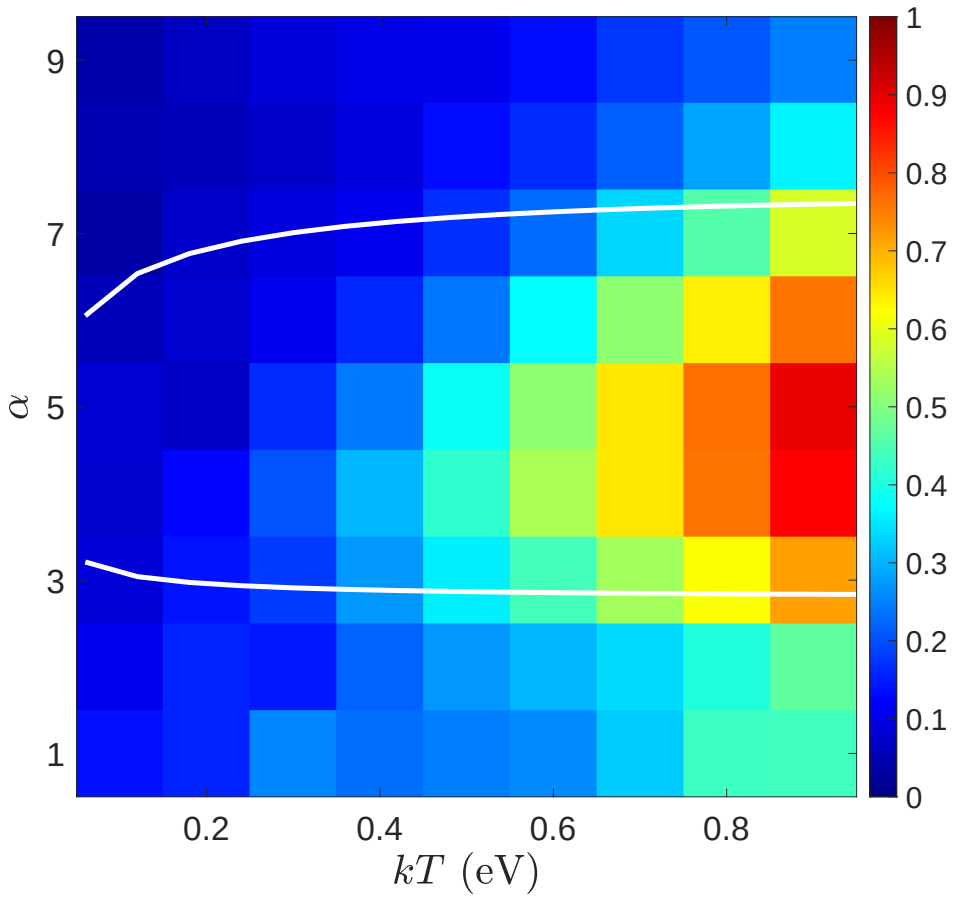

Figure 2.2: The value of order parameter ϕ as a function of temperature and aspect ratio α. The diagram is obtained by analyzing the second 5×10^6 time steps and averaging over five independent runs. White lines indicate the estimated phase boundary by solving $\Delta_m = \Delta_c$, which are described in Eq. (2.5) and Eq. (2.8), respectively.

(tilt up and tilt down) as temperature increases. A further increase in temperature will lead to the system tilting higher and staying in the tilted state longer. A close look at a typical tilt configuration shows that the sheet is not uniformly tilted along the width direction. We plot the profile of the sheet in the tilted phase in Fig. 2.3(a), and the two short free edges (marked in green in Fig. 2.1(a)) and the parallel middle line (marked in grey in Fig. 2.1(a)) in Fig. 2.3(b). It can be seen that the middle line has a pronounced buckled profile, while the two free edges have lower curvatures.

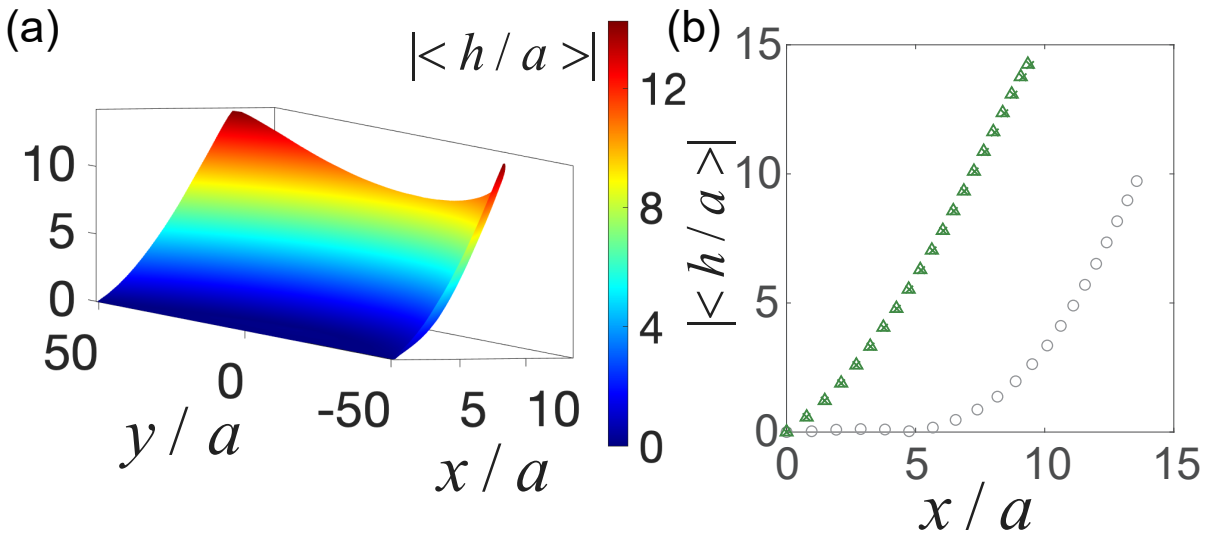

Figure 2.3: A tilted thin sheet with $kT = 0.8$eV and $\alpha = 5$. (a) Interpolated profile of the thin sheet. (b) Profile of the two short free edges (marked in green in Fig. 2.1(a)) and the parallel middle line (marked in grey in Fig. 2.1(a)).The green crosses (triangles) correspond to the top (bottom) edge, and the grey circles correspond to the midline.

2.2 Theoretical Model of Tilt

The tilted phase may be understood as a result of a buckling instability: a macroscopically flat thermalized thin sheet has a projected area smaller than its zero-temperature area due to thermally induced microscopic wrinkles (e.g. Refs. [24, 49]). The natural reference state for defining stresses and strains is the thermalized thin sheet. Thus clamping one end at its zero-temperature width W_0 exerts a stretching force along the clamped boundary. A combination of stretching and clamped boundaries is known to produce a region of compressive stress in the direction transverse to stretching, leading to a wrinkling instability in double clamped thin sheets [64, 65, 66]. In our case, a similar instability appears as tilting.

To develop an analytic model for tilt (see Appendix A for details), we use the thermalized elastic sheet as our reference state and choose the coordinates such that the ther-

malized sheet occupies the region $0 \leq x \leq L'$ and $-W'/2 \leq y \leq W'/2$, and is clamped at $x = 0$. As discussed above, a thermalized sheet is smaller than its zero-temperature counterpart, so $W' < W_0$ and $L' < L_0$. The deformation from the reference state is described by in plane displacements $u_x(\mathbf{x})$ and $u_y(\mathbf{x})$, and an out-of-plane deflection $h(\mathbf{x})$, where $\mathbf{x} = (x, y)$ [1]. The elastic energy of the system is [14]

$$E = \int d^2x \left[\frac{\kappa_R}{2} (\nabla^2 h)^2 + \mu_R u_{ij}^2 + \frac{1}{2} \lambda_R u_{kk}^2 \right], \tag{2.2}$$

where $u_{ij} = \frac{1}{2}(\frac{\partial u_i}{\partial x_j} + \frac{\partial u_j}{\partial x_i} + \frac{\partial h}{\partial x_i}\frac{\partial h}{\partial x_j})$ is the strain tensor. Thermal fluctuations renormalize the elastic moduli so that they become (strongly) scale-dependent [15, 67, 17, 20, 68, 24]: $\kappa_R(L_0) \sim \kappa \left(\frac{L_0}{l_{th}}\right)^{\eta}$ and $Y_R(L_0) = \frac{4\mu_R(\mu_R+\lambda_R)}{2\mu_R+\lambda_R} \sim Y \left(\frac{L_0}{l_{th}}\right)^{-\eta_u}$, where $\eta \approx 0.8$ and $\eta_u \approx 0.4$. Clamping imposes a boundary condition $u_x(0, y) = 0$. It also fixes the left edge to the zero-temperature width $W_0 > W'$, imposing stretching on the reference state:

$$u_y(0, \frac{W'}{2}) = -u_y(0, -\frac{W'}{2}) = \frac{W_0 - W'}{2} \equiv \frac{\epsilon}{2} W_0. \tag{2.3}$$

The extension ratio $\epsilon = (W_0 - W')/W_0$ is approximately given by [24]

$$\epsilon \approx \frac{1}{8\pi} \frac{k_B T}{\kappa} \left[\eta^{-1} - \eta^{-1} (l_{th}/L_0)^{\eta} + \ln(l_{th}/a) \right]. \tag{2.4}$$

We find it useful to double our system to the region $-L' \leq x \leq L'$ and $-W'/2 \leq y \leq W'/2$ by reflecting it about the y axis. The originally clamped edge is no longer on the boundary in this doubled system, and $u_x(0, y) = 0$ is automatically satisfied by symmetry. We consider a narrow strip with length $2L'$ around $y = 0$ and call it the middle strip, which can buckle under enough compression, serves as a simple proxy for the system in our analysis. To determine the compression Δ_m of the middle strip we

[1] We will use (x_1, x_2) interchangeably with (x, y), and (u_x, u_y) interchangeably with (u_1, u_2).

examine the system from its horizontal ($h = 0$) pre-buckled phase in Eq. (2.2). In this planar configuration, the energy functional gives the equilibrium equation for the in-plane stress $\partial_i \sigma_{ij} = 0$ [14].

On the left and right edges of the doubled system, we impose the strong traction-free boundary condition $\sigma_{xx}(\pm L', y) = 0$ and a weak boundary condition $\int \sigma_{xy}(\pm L', y) dy = 0$. On the top and bottom edges we impose $\sigma_{xy}(x, \pm W'/2) = 0$, and $\sigma_{yy}(x, \pm W'/2) = f \cos(\pi x / 2L')$, which models the stretching effect from clamping on the reference state. For simplicity, we have used a delocalized stress σ_{yy} on the boundaries instead of a highly localized stress concentrated at $x = 0$. f is determined self-consistently through the stress-strain relation by enforcing condition Eq. (2.3) on the displacement. This set of boundary conditions allows us to solve for the in-plane stress analytically with the Airy stress function method, which confirms that the middle strip is indeed subject to a compressive stress σ_{xx}.

After solving for σ_{ij} and applying the stress-strain relation, we obtain $u_{xx}(x, 0)$, which we integrate to obtain the compression Δ_m of the middle strip at $y = 0$. To first order in small ϵ we find

$$\Delta_m = -2u_x(L', 0) = \frac{L_0 \alpha \epsilon}{2\sinh^2(\frac{\pi\alpha}{4})} \Big[\frac{\pi\alpha}{4} \cosh(\frac{\pi\alpha}{4})(1+\nu_R) - \sinh(\frac{\pi\alpha}{4})(1-\nu_R) \Big] \tag{2.5}$$

where $\nu_R = \frac{\lambda_R}{2\mu_R + \lambda_R}$ is the renormalized Poisson ratio, which would be $-1/3$ for an infinitely sized, free-standing thermalized sheet [20, 68]. We observe that Δ_m crosses from negative to positive at some threshold aspect ratio (Fig. 2.4). This is due to two competing effects. The tensile stress σ_{yy} from clamping tends to extend the middle strip because of an overall negative Poisson ratio of the reference state. The compressive stress σ_{xx}, in contrast, tends to compress the middle strip. Our calculation shows that the former dominates for small aspect ratio, extending the middle strip ($\Delta_m < 0$), and the

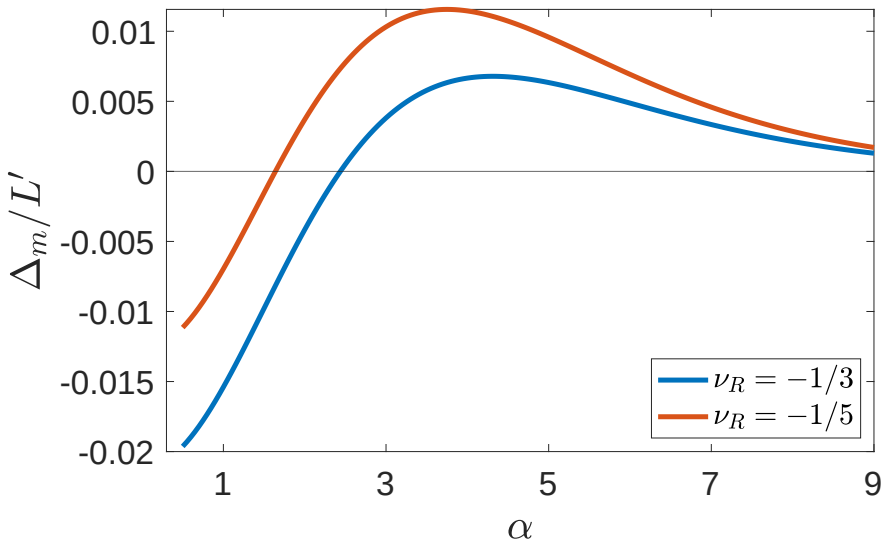

Figure 2.4: Compression of middle strip Δ_m/L' as a function of aspect ratio α using Eq. (2.5), with $\epsilon = 0.05$ and two different renormalized Poisson ratios.

latter dominates for higher aspect ratios, allowing buckling for a window of aspect ratios. For even larger aspect ratio, the two factors balance each other and Δ_m approaches zero, which implies no buckling. Note that we have analyzed the physics of a thermalized thin sheet in a mean field manner, where the effects of thermal fluctuations are only minimally incorported through the renormalization of elastic moduli. A finite element calculation in the same spirit using the FEniCS package [69] and a comparison between MD simulation, theory and finite element calculation is presented in Appendix A.

To estimate the critical compression Δ_c above which the sheet buckles we use a one dimensional model for the middle strip. Dropping the y derivatives and u_y in Eq. (2.2), we have an energy density functional

$$\mathcal{E}[u_x, h] = \frac{\kappa_R}{2}\int dx \left(\frac{d^2h}{dx^2}\right)^2 + \frac{Y_R}{2(1-\nu_R^2)}\int dx \left[\frac{du_x}{dx} + \frac{1}{2}\left(\frac{dh}{dx}\right)^2\right]^2 \tag{2.6}$$

with the anti-periodic boundary condition $u_x(-L') = -u_x(L') = \Delta/2$ on the displace-

ment. The integration is implied to be from $x = -L'$ to $x = L'$. Integrating out the displacement field gives an effective energy density in terms of h alone:

$$\begin{aligned}
\mathcal{E}_{eff}[h] &= -k_B T \ln\left[\int Du_x e^{-\mathcal{E}[u_x,h]/k_B T}\right] \\
&= \frac{\kappa_R}{2}\int dx\left(\frac{d^2h}{dx^2}\right)^2 + \frac{Y_R}{4L'(1-\nu_R^2)}\left[\Delta - \frac{1}{2}\int dx\left(\frac{dh}{dx}\right)^2\right]^2 \\
&= \frac{\kappa_R}{2}\int dx\left(\frac{d^2h}{dx^2}\right)^2 - \frac{Y_R}{2(1-\nu_R^2)}\frac{\Delta}{2L'}\int dx\left(\frac{dh}{dx}\right)^2 \\
&+ \frac{Y_R}{2(1-\nu_R^2)}\frac{1}{8L'}\int\int dxdx'\left(\frac{dh}{dx}\right)^2\left(\frac{dh}{dx'}\right)^2,
\end{aligned} \tag{2.7}$$

where we drop a constant term independent of h from the second line. A quartic term similar to the one in the last line also appears in a circular plate under strain imposed on the boundary [52]. We use a mean field variational function $h(x) = H\cos\left(\frac{\pi x}{2L'}\right)$, where H serves as the buckling order parameter whose behavior depends on Δ. If minimization of Eq. (2.7) requires $H = 0$, the strip will stay in the plane; if it requires $H \neq 0$, then the strip will buckle out of the plane. The boundary between these two behaviors define the critical compression, which is calculated to be

$$\Delta_c = \frac{\pi^2}{2L'}\frac{\kappa_R(1-\nu_R^2)}{Y_R}. \tag{2.8}$$

Setting $\Delta_m = \Delta_c$, and combining the results of Eq. (2.4), Eq. (2.5) and Eq. (2.8), we obtain the phase boundary between the horizontal and tilted phases, which is shown with thick white lines in Fig. 2.2. The result shows that the tilted phase exists for a finite window of aspect ratios, consistent with our MD simulations. Here we have used a constant $\nu_R = -1/3$ which is the universal Poisson ratio for an infinitely sized, free-standing thermal sheet [20, 68]. Finite-size effects and the suppression of thermal fluctuations from clamping may shift ν_R to a less negative value and even introduce

spatial and strain dependence. We leave such complications to further studies and only point out that a less negative Poisson ratio such as $\nu_R = -1/5$ reduces the effect of the tensile σ_{yy} and favors compression of the middle strip, as can be seen from Fig. 2.4, but does not qualitatively change our conclusions. Our study shows that the compressive stress induced by thermal fluctuation and clamped boundary can overcome a negative Poisson's effect and lead to buckling.

The observation that tilt is only present for $kT \gtrsim 0.4$eV in MD simulations is a non-universal result of the small system size, and we expect larger systems to favor tilt for the following reason: Eq. (2.5) gives $\Delta_m \sim L_0$, and Eq. (2.8) gives $\Delta_c \sim L_0^{-1+\eta+\eta_u} \approx L_0^{0.2}$. The amount of compression of the middle strip therefore grows much faster than the critical compression required for tilting as system size increases. A comparison of the phase diagrams of $L_0 = 20a$ and $L_0 = 30a$ suggests that tilt is more easily observed for larger systems (see Appendix A). We also observe tilt, for instance, with $L_0 = 60a$, $\alpha = 5$ at $k_BT = 0.1eV$, with an order parameter $\phi \approx 0.47$. We expect a much lower tilt temperature for real experiments with larger samples, where L_0 can be orders of magnitude greater than the microscopic lattice spacing.

Chapter 3

Effective Moduli of Disordered Odd Elastic Lattices

Odd elasticity is characterized by a stress-strain relation incompatible with conservation of energy [13]. In the Hookean approximation, the stress and strain in an odd elastic material are related by a non-symmetric elastic tensor. The absence of a potential energy gives rise to peculiar phenomena in odd elastic materials, including work-extraction under deformation cycles, self-sustained waves in the bulk in the over-damped limit [13], and non-Hermitian topological skin effects [70, 71]. Experimentally, odd elasticity has been reported in a robotics system with piezoelectric elements [72], in a colloidal spinners system [73], and in assemblies of spinning bacteria [74] and starfish embryos which exhibit self-sustained chiral waves [75]. Violation of energy conservation in these example systems is achieved by external supplies of energy consumed by particles in the systems locally, a signature of a broad class of systems known as active matter [34]. Simulations and calculations from Ref. [76], however, suggest that odd elasticity can also arise from passive chiral elements. Despite this subtlety, for the sake of simplicity, we refer to any elasticity that is not odd as passive in this thesis.

Considering the potential for extracting work from engines built with odd elastic materials and the use of odd elasticity for designing novel robots, it is natural to ask what are the effects of disorder on an odd elastic medium. How robust is odd elasticity in the face of disorder? How do the odd elastic moduli behave if certain electronic components in an artificial odd system malfunction? Does disorder induce a passive-to-odd phase transition? These questions may also be relevant in the context of the starfish embryos experiment in Ref. [75]. As embryos develop, their mutual interaction suffers an increase of effective noise, which leads to an eventual dissolution of the odd crystals. Studying disorder may shed light on the properties of the odd elastic crystals in the intermediate to long time scale.

Here, we investigate the impact of bond disorder on the odd moduli of thin sheets represented by two-dimensional triangular and honeycomb lattices, where each spring has a probability p of being odd. We find that oddness is robust against disorder, and it persists at small p, i.e. there is no passive-to-odd phase transition at a finite p. We show that the behavior of odd moduli as a function of p is the result of a competition between the affine response of the passive elastic backbone and a rigidity percolation transition in the odd elastic components.

3.1 Disordered Odd Elastic Lattices

We study two types of two-dimensional lattices: triangular lattices and honeycomb lattices, which are illustrated in Fig. 3.1. For triangular lattices, we impose that each bond is at least a passive spring with a spring constant k. Additionally, each spring has a probability p of having an odd spring constant k^o. To reiterate the exposition from Chapter 1, an odd spring with a rest length a connecting particles at $\mathbf{r}_1$ and $\mathbf{r}_2$ exerts a

force

$$\mathbf{F} = -\left(k\frac{\Delta\mathbf{r}}{|\Delta\mathbf{r}|} + k^o\frac{\Delta\mathbf{r}^*}{|\Delta\mathbf{r}^*|}\right)(|\Delta\mathbf{r}| - a) \tag{3.1}$$

on the particle at $\mathbf{r}_1$, where k is the passive spring constant and k^o the odd spring constant. $\Delta\mathbf{r} = \mathbf{r}_1 - \mathbf{r}_2$ is the positional separation between the two particles, and $\Delta\mathbf{r}^* = \boldsymbol{\epsilon}\cdot\Delta\mathbf{r}$, where $\boldsymbol{\epsilon}$ is the two-dimensional Levi-Civita tensor. Throughout this chapter and Appendix B, we use a dot to denote multiplication between a matrix and a vector, as well as to indicate the inner product between two vectors. When two vectors are juxtaposed without a dot in between,, they are multiplied in an outer product to form a matrix.

A honeycomb lattice is a triangular lattice where each unit cell hosts two particles, distinguished by blue and red colors in Fig. 3.1(b). Nearest-neighbor (NN) springs connect type A particles to type B particles, forming a tiling of regular hexagons. Next-nearest-neighbor (NNN) springs connect particles of the same type, resulting in an NNN network that is comprised of two overlapping triangular lattices. In our disordered models, each NN and NNN spring has a passive spring constant k. An NN spring has a probability p of having an odd spring constant k_1^o, while an NNN spring has a probability p of having k_2^o. For both lattices, the probability distribution of disorder is independent from one spring to another.

At the disorder-free $p = 1$ limit, both lattices are isotropic odd elastic materials. In the continuum limit, under the Hookean approximation, the coarse-grained stress and strain fields are related by a non-symmetric elastic tensor. As introduced in Chapter 1, we can represent stress in terms of four independent components of pressure (σ^0), torque density (σ^1), shear stress 1 (σ^2) and shear stress 2 (σ^3). Similarly, we represent strain with the corresponding components u^α of dilation, rotation, and the two shear strains.

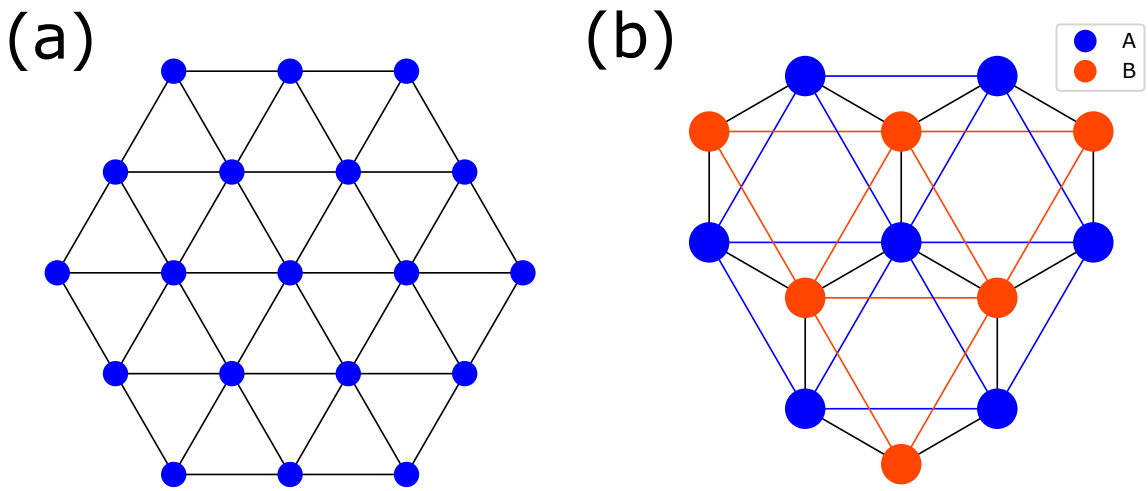

Figure 3.1: Illustration of the geometric structure of the triangular (a) and honeycomb (b) lattice models.

The stress-strain relation is given by:

$$\begin{pmatrix} \sigma^0 \\ \sigma^1 \\ \sigma^2 \\ \sigma^3 \end{pmatrix} = \begin{pmatrix} B & 0 & 0 & 0 \\ A & 0 & 0 & 0 \\ 0 & 0 & \mu & K^o \\ 0 & 0 & -K^o & \mu \end{pmatrix} \begin{pmatrix} u^0 \\ u^1 \\ u^2 \\ u^3 \end{pmatrix}, \tag{3.2}$$

where we have omit writing the spatial dependence of the stress and strain fields. Here, B is the passive bulk modulus, and μ is passive the shear modulus. For triangular lattices, $B = 2\mu = \sqrt{3}k/2$, and for honeycomb lattices, $B = (k_1 + 6k_2)/(2\sqrt{3})$ and $\mu = \sqrt{3}k_2/2$. The odd modulus K^o couples shears in different directions in a non-reciprocal way, violating the conservation of energy. The odd modulus A couples dilation to an internal torque density, violating both the conservation of energy and the conservation

of angular momentum. For triangular lattices,

$$A = 2K^o = \frac{\sqrt{3}}{2}k^o. \tag{3.3}$$

For honeycomb lattices,

$$\begin{aligned} A &= \frac{k_1^o + 6k_2^o}{2\sqrt{3}} \\ K^o &= \frac{\sqrt{3}}{2}k_2^o. \end{aligned} \tag{3.4}$$

One can therefore fine-tune the value of A independent of K^o by choosing appropriate k_1^o. In this chapter, we fix $(k_1^o/k_2^o) = -6$ so that $A = 0$ at $p = 1$. That is, at the disorder-free limit, angular momentum is conserved. The objective of our study is to determine how the measured values of the odd moduli change as functions of p. We denote the measured, or effective, odd moduli of the disordered lattices as A_m and K_m^o, and we will use both a mean field theory and numerical simulations to determine A_m and K_m^o.

3.2 Overview of Effective Medium Theory

We study the disordered lattices with a well-established effective medium theory (EMT) with the coherent potential approximation [77]. EMT is an uncontrolled mean field method where we map the disordered system to a disorder-free effective medium whose parameters are determined self-consistently [78, 79]. The form of EMT described below has been successfully applied to problems in various contexts [80, 81, 82], and can be adapted to systems with dynamics not derived from an energy function.

The configuration of an elastic lattice in two dimensions is describe by a $2nN$-dimensional displacement vector $\mathbf{u}$, where N is the number of unit cells in the lattice, and n is the number of particles per unit cell. The forces on the particles are encoded into a $2nN$-dimensional vector $\mathbf{F}$. Under the Hookean approximation, the two vectors

are linearly related:

$$\mathbf{F} = -\mathbf{D} \cdot \mathbf{u}, \tag{3.5}$$

where $\mathbf{D}$ is the dynamical matrix, which is a function of the microscopic spring constants and disorder. The static Green's function $\mathbf{G}$ is defined as the negative inverse of the dynamical matrix:

$$\mathbf{G} = -\mathbf{D}^{-1}. \tag{3.6}$$

We use the triangular lattice to outline the general procedure of EMT, and direct readers to Appendix B for detailed calculations. Instead of studying the full disordered Green's function $\mathbf{G}$, EMT seeks to describe the disordered system with an effective homogeneous (disorder-free) medium with a dynamical matrix $\mathbf{D}_m$, and Green's function $\mathbf{G}_m = -(\mathbf{D}_m)^{-1}$. The dynamical matrix $\mathbf{D}_m$ is a function of the effective odd spring constant k_m^o, which varies with p and is generally not equal to k^o. The determination of k_m^o follows this approach: we replace one of the springs in the effective medium by a disordered spring with an odd elastic constant k_s^o. The replacement spring is sampled from the same disorder probability distribution in the original disordered system. Therefore, k_s^o is a random variable with the following distribution:

$$P(k_s^o) = p\,\delta(k_s^o - k^o) + (1-p)\,\delta(k_s^o). \tag{3.7}$$

This replacement corresponds to a perturbation matrix $\mathbf{V}$ to the dynamical matrix $\mathbf{D}_m$. The perturbed dynamical matrix is then $\mathbf{D}' = \mathbf{D}_m + \mathbf{V}$. Inverting this expression, one can show that the perturbed Green's function of the effective medium is:

$$\mathbf{G}' = \mathbf{G}_m + \mathbf{G}_m \cdot \mathbf{T} \cdot \mathbf{G}_m, \tag{3.8}$$

where

$$\begin{aligned}\mathbf{T} &= \mathbf{V} \cdot (\mathbf{I} - \mathbf{G}_m \cdot \mathbf{V})^{-1} \\ &= \mathbf{V} + \mathbf{V} \cdot \mathbf{G}_m \cdot \mathbf{V} + \mathbf{V} \cdot \mathbf{G}_m \cdot \mathbf{V} \cdot \mathbf{G}_m \cdot \mathbf{V} + ...\end{aligned} \tag{3.9}$$

is called the T-matrix, and $\mathbf{I}$ is the identity matrix. Since the effective medium is a faithful representation of the original disordered system, the replacement of a single spring with a spring sampled from the original disorder probability distribution should, on average, have no impact on the effective medium's Green's function. We therefore impose $\langle \mathbf{G}' \rangle = \mathbf{G}_m$, where the average is taken over the probability distribution in Eq. (3.7). A self-consistent solution to this requirement is

$$\langle \mathbf{T} \rangle = 0, \tag{3.10}$$

which turns out to be a single equation for the one unknown k_m^o. In this treatment, we disregard any deviation of the effective passive spring constant from its disorder-free value, which has been numerically tested to be at most a few percent.

3.3 Numerical Simulation Methods

We also study the problem with molecular dynamics simulations. For both triangular and honeycomb lattices, we setup $n_1 = 30$ rows and $n_2 = 31$ columns of unit cells where the springs obey force law in Eq. (3.1) and exhibit disorder as described in the previous sections. To measure the elastic moduli, we first apply a small global compression or shear with an affine displacement $\mathbf{u}_i^{\text{aff}} = \boldsymbol{\eta} \cdot \mathbf{x}_i$, where $\boldsymbol{\eta}$ is a 2 by 2 matrix. Here, the i subscript indexes the vertices in the lattice, and $\mathbf{x}_i$ is the equilibrium position of the particle on the i-th vertex. For compression, $\boldsymbol{\eta} = -\gamma \mathbb{I}_2$, where $\mathbb{I}_2$ is the two-dimensional

identity matrix. For shear,

$$\boldsymbol{\eta} = \gamma \begin{pmatrix} 1 & 0 \\ 0 & -1 \end{pmatrix}, \tag{3.11}$$

which corresponds to shear strain 1. In all simulations, we choose $\gamma = 0.01$.

To maintain a constant overall strain, we do not time-evolve positions of particles on the boundary after applying the initial distortion. We time-evolve positions of particles in the interior of the system, following the over-damped dynamics given by:

$$\lambda \frac{d}{dt}\mathbf{r}_i(t) = \mathbf{F}_i(t), \tag{3.12}$$

where $\mathbf{F}_i$ is the force on particle i, which depends on the positions of its neighboring particles. We use the lattice spacing of the triangular lattices as the unit of length, and λ/k as the unit of time, where k is the passive spring constant. The system dynamics are integrated using a second order Runge-Kutta method for 10^4 time steps, with a time step of $dt = 0.001$. We then measure the microscopic stress tensor in the bulk, whose value at the position of particle i is [83, 84]:

$$\boldsymbol{\sigma}_i = \frac{1}{2A} {\sum_j}' (\mathbf{r}_j - \mathbf{r}_i)\mathbf{F}_{ij}, \tag{3.13}$$

where the sum is over particles j connected to particle i. A is the area occupied by particle i, which, in the small strain limit, is independent of i and equals the area of a unit cell in triangular lattices and half of the area of a unit cell in honeycomb lattices. $\mathbf{F}_{ij}$ is the force on particle i due to its connection with particle j. The separation vector $(\mathbf{r}_j - \mathbf{r}_i)$ and the force vector $\mathbf{F}_{ij}$ are multiplied in an outer product on the right hand side. With this definition of stress tensor, we have $\mathbf{T} = \mathbf{n} \cdot \boldsymbol{\sigma}$, where $\mathbf{T}$ is the external force on a surface element with surface normal vector $\mathbf{n}$. Using Eq. (3.2), we extract the

elastic moduli from the imposed overall strain and the spatial average of the microscopic stress tensor. All elastic moduli are measured in units of the passive spring constant k, and we omit writing k below. We also calculate a non-affine parameter Γ for the final configuration of each simulation run, defined as:

$$\Gamma = \frac{1}{N\gamma^2} \sum_i |\mathbf{u}_i - \mathbf{u}_i^{\text{aff}}|^2. \tag{3.14}$$

This parameter quantifies how far the final configuration deviates from the initially imposed affine distortion [85]. We perform ten independent simulation runs for each choice of parameter. Given the consistent agreement between the results of EMT and molecular dynamics simulations, we present their findings collectively below.

3.4 Results

3.4.1 Triangular Lattices

For triangular lattices, Eq. (3.10) leads to an equation for k_m^o:

$$k_m^o = k^o \frac{p - H(k_m^o)}{1 - H(k_m^o)}, \tag{3.15}$$

where

$$H(k_m^o) = \frac{2}{3} \frac{(k_m^o)^2}{1 + (k_m^o)^2}. \tag{3.16}$$

After some arithmetic, we observe that Eq. (3.15) reduces to a cubic equation with a unique solution $k_m^o > 0$ for any probability $p > 0$. This result implies that even the slightest presence of odd springs in our setup makes the system odd as a whole. This is a natural consequence of the design, since every odd spring breaks conservation of energy locally with a chiral force, and all odd spring in the setup have the same sign of k^o, and

hence the same sign of chirality. When the system is compressed, for instance, we expect all odd springs to experience some degree of compression. Since they possess identical chirality, they collectively generate torques in the same direction locally, leading to a non-zero internal torque globally. The uniform chirality is crucial as one can imagine that in a setup where each odd spring has an equal probability of having k^o or $-k^o$, the system as a whole may not be odd elastic on average.

We now examine $K^o_m = A_m/2 = \sqrt{3}k^o_m/4$ as a function of p and k^o in a few limiting regimes. Near $p = 0$, we expect that $k^o_m \ll 1$. Solving Eq. (3.15) in this regime gives

$$\frac{K^o_m}{K^o} = \frac{k^o_m}{k^o} \approx p - \frac{2}{3}(k^o)^2 p^2. \tag{3.17}$$

That is, the scaled effective oddness is locally a concave function of p, and its curvature increases as a function of oddness k^o. Based on a counting argument by Maxwell [86], we expect the odd springs in the disordered lattice to form a system-spanning rigid cluster close to $p = 2/3$. At $p = 2/3$, Eq. (3.15) gives $(K^o_m/K^o) \approx 2/3 = p$ for $k^o \ll 1$, and $(K^o_m/K^o) \sim (k^o)^{-2/3}$ for $k^o \gg 1$. The scaled effective oddness, therefore, *decreases* as a function of k^o at $p = 2/3$. Lastly, near the disorder-free point, expanding to linear order in $\delta p = 1 - p$, we get

$$\delta K^0_m = K^o - K^o_m \approx K^o \, \frac{3(k^o)^2 + 3}{(k^o)^2 + 3} \, \delta p, \tag{3.18}$$

where the fraction on the right hand side is an increasing function of k^o. From these simple calculations, we come to the conclusion that for a small k^o, the scaled effective oddness K^o_m/K^o increases almost linearly with p. In contrast, for a larger k^o, K^o_m/K^o increases slowly at small p, and increases faster after some probability around $p = 2/3$. These features are consistent with molecular dynamics simulations results and numerical

solutions of Eq. (3.15), presented collectively in Fig. 3.2.

To understand the above results qualitatively, we consider two limiting scenarios. In the limit of small k^o, the elastic property of a disordered lattice is controlled predominately by the passive elastic backbone, which responds to a small global distortion affinely. Under a global compression, for instance, the odd springs are compressed by almost the same amount, and the total internal torque generated scales linearly with the percentage of odd springs in the system. This results in a linear relation between K_m^o and p for $k^o \ll 1$. In the large k^o limit, the response of the system is controlled by the odd components in the lattice, which undergo a rigidity percolation transition near $p = 2/3$ [86]. Below the critical rigidity percolation probability, there is little elastic response, passive or odd, and we expect K_m^o to be near zero for $p < 2/3$, before ramping up as a function of p for $p > 2/3$. The actual behavior of K_m^o at intermediate values of oddness is then a crossover between these two limits. Further confirming our interpretation, the probability p at which K_m^o/K^o deviates the most from linearity is near $p = 2/3$, similar to a passive rigidity percolation transition [78], as shown in Fig. 3.2(b). This observation, however, does not imply that the non-affine parameter Γ of the system is the greatest at this value. Indeed, as shown in Fig. 3.3(a, b), the non-affine parameter for both sheared and compressed disordered triangular lattices is maximized at a lower value of p, and is dependent on k^o. In some models of disordered elastic media, non-affine response is strongly correlated with the softening of effective passive elastic moduli [87]. In this case, however, it does not appear to have a correlation with the behavior of effective odd moduli. Predicting Γ as a function of p is beyond the capability of EMT, since the effective medium is disorder-free.

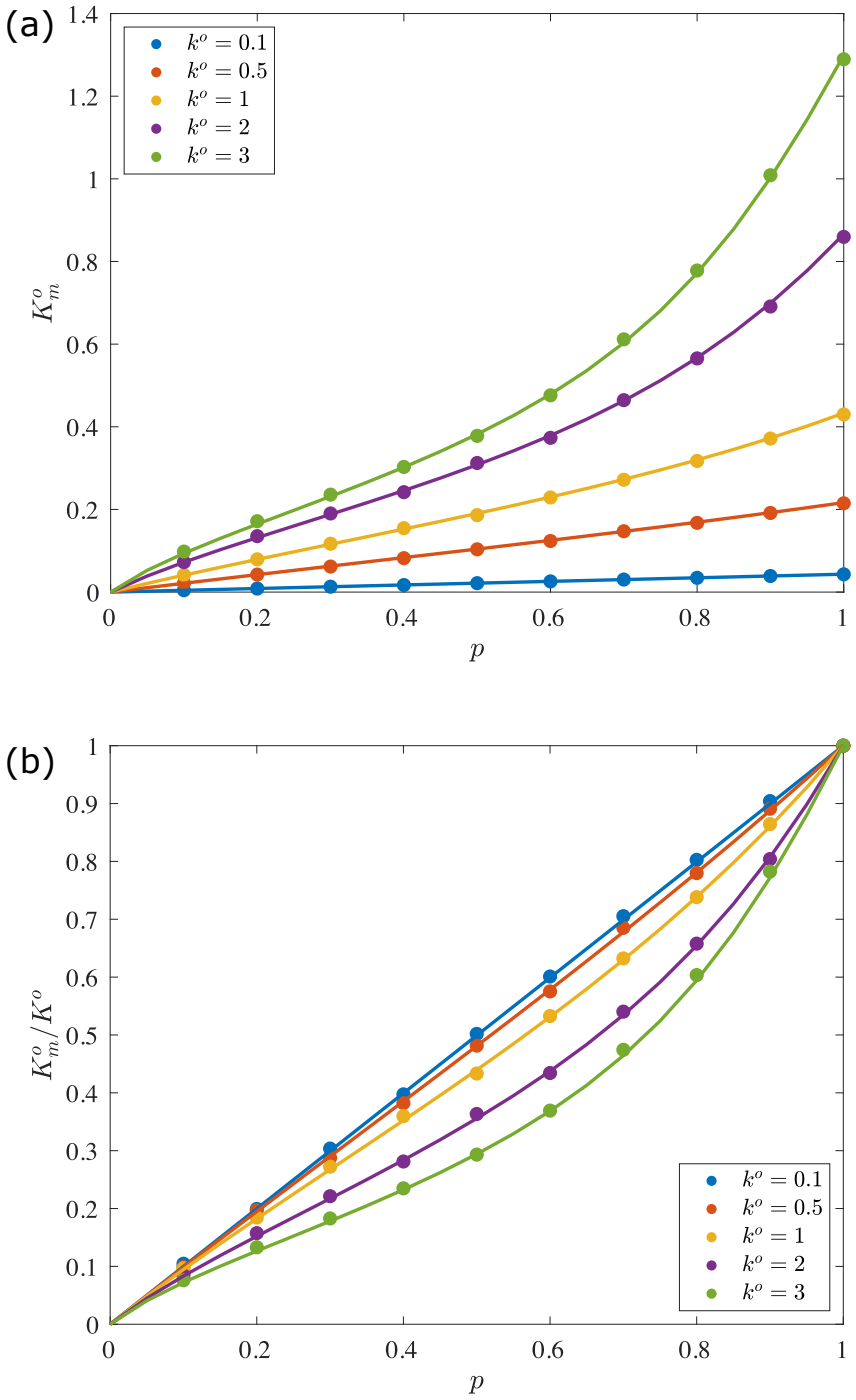

Figure 3.2: Effective odd modulus K_m^o, unscaled (a) and scaled (b) as a function of probability p, for triangular lattices with different values of k^o. Numerical solutions of Eq. (3.15) are plotted with solid curves, and molecular dynamics simulations results are presented with dots. Error bars are smaller than the dot size.

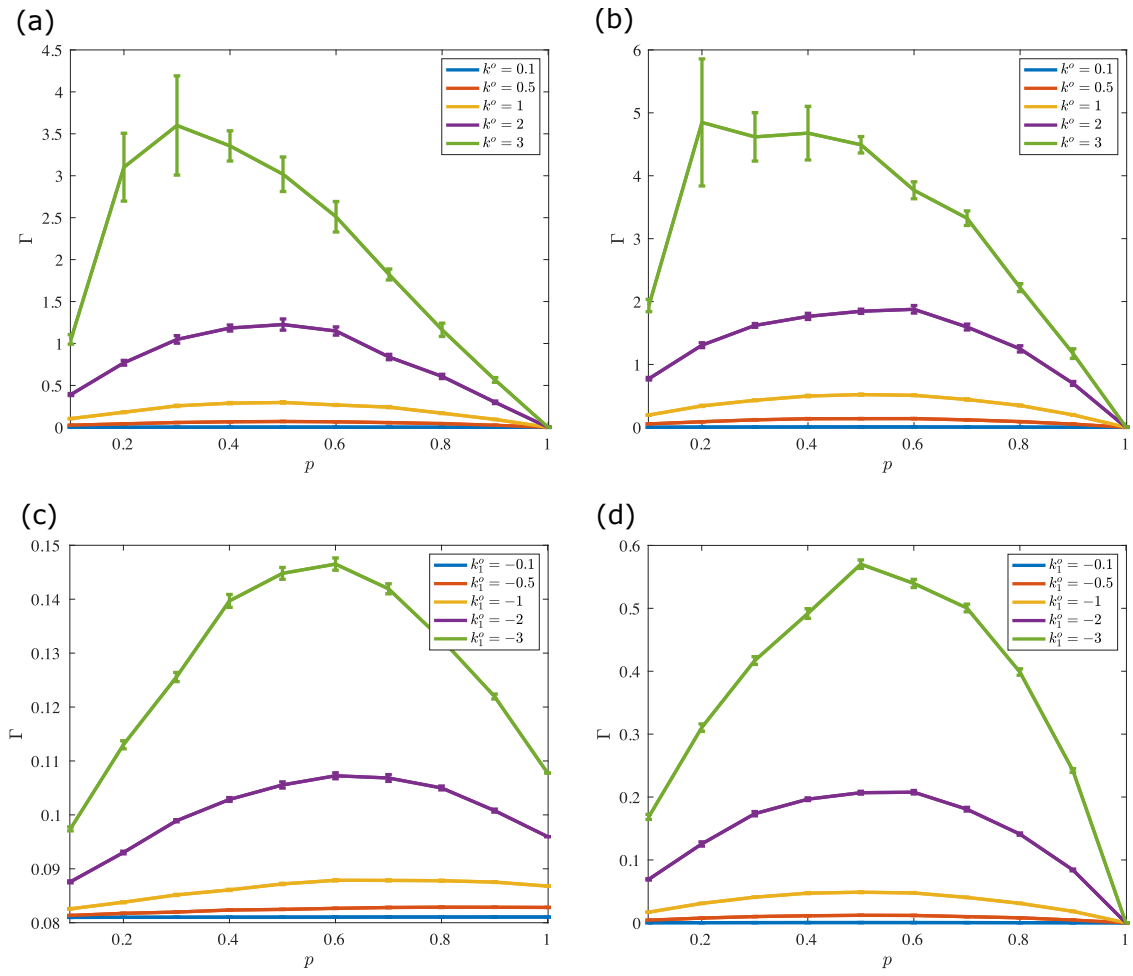

Figure 3.3: Non-affine parameter Γ for triangular lattices (top row) and honeycomb lattices (bottom row) with an initial global shear (left column) and compression (right column) distortion.

3.4.2 Honeycomb Lattices

For honeycomb lattices, we have two EMT equations, one for NN springs and the other for NNN springs. These equations are:

$$\begin{aligned} k^o_{1,m} &= k^o_1 \frac{p - H_1(k^o_{1,m}, k^o_{2,m})}{1 - H_1(k^o_{1,m}, k^o_{2,m})} \\ k^o_{2,m} &= k^o_2 \frac{p - H_2(k^o_{1,m}, k^o_{2,m})}{1 - H_2(k^o_{1,m}, k^o_{2,m})}. \end{aligned} \tag{3.19}$$

The effective odd spring constants are coupled through functions $H_1(k^o_{1,m}, k^o_{2,m})$ and $H_2(k^o_{1,m}, k^o_{2,m})$. These functions have no convenient closed form expressions, in contrast to the one for triangular lattices, and we present their derivation in Appendix B. Despite such complication, we can expect that in general, $H_1(k^o_{1,m}, k^o_{2,m}) \neq H_2(k^o_{1,m}, k^o_{2,m})$, and Eq. (3.19) implies $(k^o_{1,m}/k^o_{2,m}) \neq (k^o_1/k^o_2)$ for $p < 1$. This means that even though we choose $k^o_1/k^o_2 = -6$, making our system torque-free with $A = (k^o_1 + 6k^o_2)/(2\sqrt{3}) = 0$ at $p = 1$, this feature and, in general, any fine-tuned ratio between A and K^o, are not robust in the presence of disorder.

We solve Eq. (3.19) numerically and the results compare well with molecular dynamics simulations, as shown in Fig. 3.4. The odd modulus K^o_m is nearly a linear function of p, and A_m is non-zero in general as expected, and is maximized near $p = 0.6$. These findings align with our intuition derived from triangular lattices. First, recall that $K^o_m = \sqrt{3}\, k^o_{2,m}/2$ is completely determined by the NNN springs, which form two overlapping triangular lattices. Given that $k^o_2 \leq 1/2$, the almost linear growth of K^o_m with respect to p across all simulations is expected. As in the triangular lattices, for $|k^o_1| \ll 1$, we also expect $k^o_{1,m}$ to be linear in p, making $A_m = (k^o_{1,m} + 6k^o_{2,m})/(2\sqrt{3}) \approx p\,(k^o_1 + 6k^o_2)/(2\sqrt{3}) = 0$, as shown in Fig. 3.4(b). At larger values of $|k^o_1|$, we expect $k^o_{1,m}$ to be a nonlinear function of p, satisfying $k^o_{1,m}(p)/k^o_1 < p$, similar to the behavior seen in Fig. 3.2(b). Combining

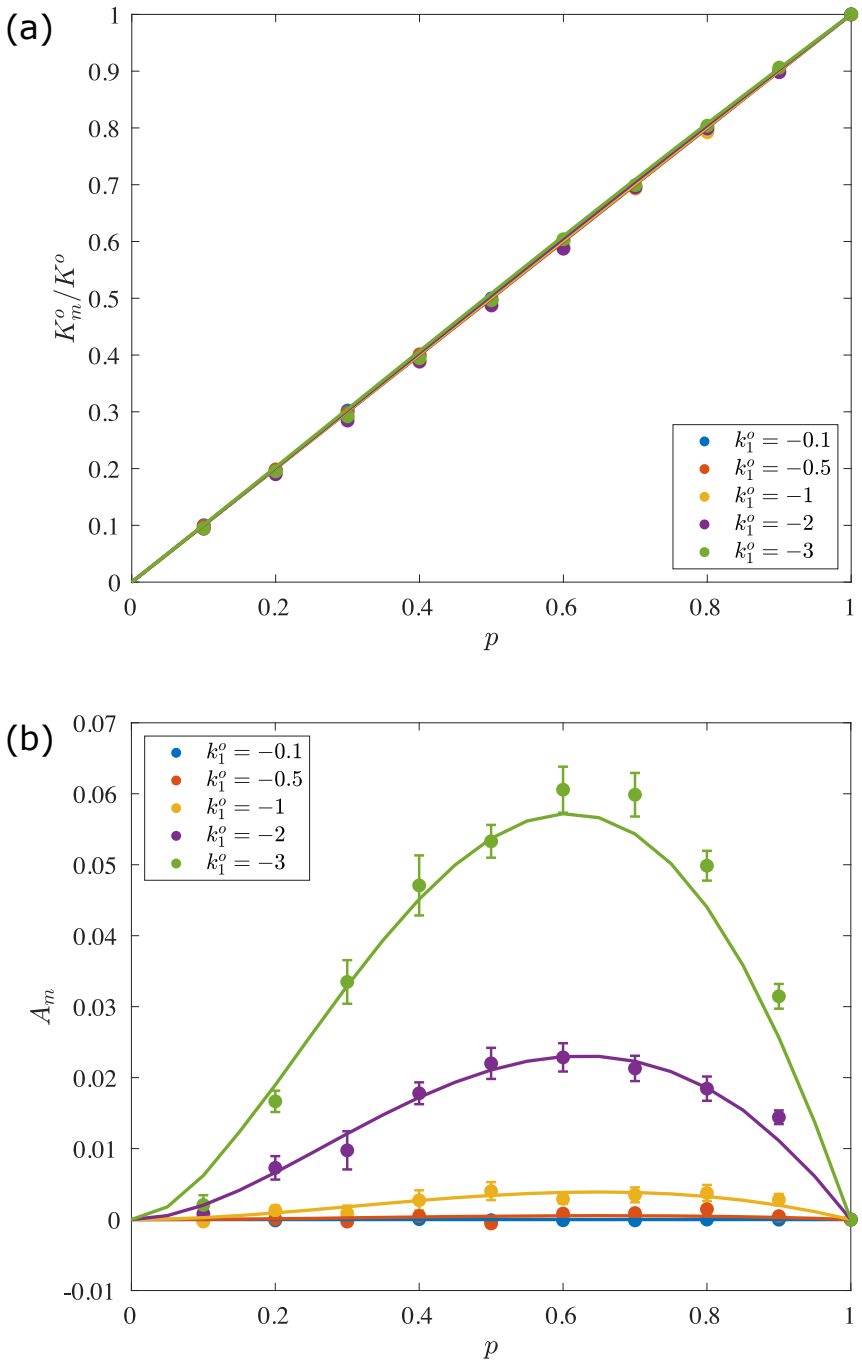

Figure 3.4: Effective odd modulus K_m^o (a) and A_m (b) in disordered odd honeycomb lattices, at different values of k_1^o, with a fixed ratio $k_1^o/k_2^o = -6$. Numerical solutions of Eq. (3.19) are plotted with solid curves, and molecular dynamics simulations results are presented with dots.

the nonlinearity of $k^o_{1,m}$ and linearity of $k^o_{2,m}$ in this regime, we expect A_m to be a positive nonlinear function of p, reaching its maximum at a value of p at which $k^o_{1,m}$ deviates from linearity the most. Therefore, even though $k^o_{1,m}$ and $k^o_{2,m}$ are coupled in the EMT equations, we can understand the results of honeycomb lattices qualitatively by considering them independently. Finally, we observe that the non-affine parameter Γ in honeycomb lattices has similar features as in triangular lattices, as shown in Fig. 3.3. At low p, Γ increases as a function of p due to disorder, and it decreases to zero (a smaller value) at $p = 1$ for a compressed (sheared) honeycomb lattice.

Our study reveals that odd elasticity, characterized by a non-symmetric elastic tensor, is robust against disorder, albeit with the disruption of certain fine-tuned features. Our results offer a practical diagnostic tool: by measuring the residual oddness, one can estimate the operational fraction of odd springs in a system. In the context of the experiment in Ref. [75], where starfish embryo crystals dissolve in time, our findings predict that enforcing crystallization of a dissolving embryo collection by external constraint results in a crystal that may still be odd elastic. Such an experiment would further confirm the odd elasticity of the living crystals.

Appendix A

Supplemental Material for Chapter 2

A.1 Molecular Dynamics Simulations

In thin sheet elasticity theory the elastic energy is given by the sum of stretching and bending terms [14, 88]: $E_{el} = E_s + E_b$. For a discrete triangulation the stretching energy is

$$E_s = \frac{\varepsilon}{2} \sum_{\langle ij \rangle} \left(|\mathbf{r}_i - \mathbf{r}_j| - a \right)^2 , \tag{A.1}$$

and the bending energy is

$$E_b = \frac{\tilde{\kappa}}{2} \sum_{\langle IJ \rangle} \left(\hat{\mathbf{n}}_I - \hat{\mathbf{n}}_J \right)^2 , \tag{A.2}$$

where ε is the discrete spring constant, a is the equilibrium spring length and $\tilde{\kappa}$ is the discrete bending modulus. As usual $\langle ij \rangle$ denotes pairs of nearest-neighbor vertices, with positions $\mathbf{r}_i$ in the 3D Euclidean embedding space and $\langle IJ \rangle$ denotes pairs of triangular plaquettes sharing a common edge, with $\hat{\mathbf{n}}_I$ being their unit normals. The corresponding continuum moduli are $Y = 2\varepsilon/\sqrt{3}$, $\kappa = \sqrt{3}\tilde{\kappa}/2$ and zero-temperature Poisson ratio $\nu = 1/3$ [55, 56, 57]. The lattice constant a can be taken as the distance between neighboring hexagons when describing the dual honeycomb lattice applicable to graphene.

This discretized model has been used to study a wide variety of 2D elastic membranes (see Ref. [49]). With graphene as a concrete example, we set the equilibrium spring length a to be $\sqrt{3}a_0$, where $a_0 = 1.42\,\text{Å}$ is the carbon-carbon bond length in graphene – thus $a \approx 2.46\,\text{Å}$, where we again note that the triangular lattice we employ is the dual of graphene's honeycomb lattice. To give the correct graphene density we take the mass of every vertex to be $m = 2m_C \approx 4 \times 10^{-26}$ kg, where m_C is the mass of a carbon atom. We choose a and m as our units of length and mass and set $a = 1$ and $m = 1$ in all simulations. Fig. 2.1(a) displays the initial, zero-temperature flat configuration of the elastic sheet in the $x - y$ plane, with $n_1 = 21$ vertices in the short (x) direction and $n_2 = 117$ vertices staggered along the long (y) direction. Therefore, $L_0 \approx 20a \approx 50$Å and $W_0 = 58\sqrt{3}a \approx 100$Å. There are 2399 vertices in total. We perform MD simulations using both the HOOMD-blue [60, 59] and the LAMMPS software packages [61] and find consistent results. We choose $E_0 = 1\,\text{eV}$ as the unit of energy in all simulations. The elastic energy is calculated as the sum of the stretching and bending energies given in Eqs. (A.1) and (A.2), with bare elastic parameters $\kappa = 1.2\,\text{eV}$ [58, 26] and $Y = 20\,\text{eV/Å}^2$ [27, 28] for graphene. The discrete parameters ε and $\tilde{\kappa}$ follow from the relations above. After giving the free vertices a small random out-of-plane displacement, we update their positions in the constant temperature (NVT) ensemble. The simulation unit of time thus corresponds to a real time $t_0 = \sqrt{m\,a^2/E_0} \approx 0.12$ps. Finally we set the integration timestep to be 0.005. Every simulation timestep τ thus corresponds to a real time $\tau = 0.005\,t_0 \approx 0.6\,\text{fs}$. Every simulation run consists of 10^7 time steps in total, with the first 5×10^6 time steps ensuring equilibration. For data analysis we record one configuration every 10^4 time steps in the second 5×10^6 timesteps.

We plot the phase diagram of a system with $L_0 = 30a$ in Fig. A.1. To compare with the system of $L_0 = 20a$ presented in Chapter 2, we plot in Fig. A.1(a) the order parameter on the same colorbar scale as Fig. 2.2. We see that with a larger system

size, the region for the tilted phase is larger. Fig. A.1(b) plots the same phase diagram with colorbar scaled to data, from which we see that the order parameter reaches larger values for $L_0 = 30a$, indicating a more pronounced tilt. The tilt region here seems to correspond to slightly higher aspect ratios compared to Fig. 2.2. The optimal aspect ratio where the tilt order parameter is maximized, is between 4 and 5 for simulations with $L_0 = 20a$, depending on temperature, and it is mostly between 5 and 6 for simulations with $L_0 = 30a$. However, for $L_0 = 30a$ with the highest simulated temperature, the tilt order parameter is maximized at an aspect ratio of 7.

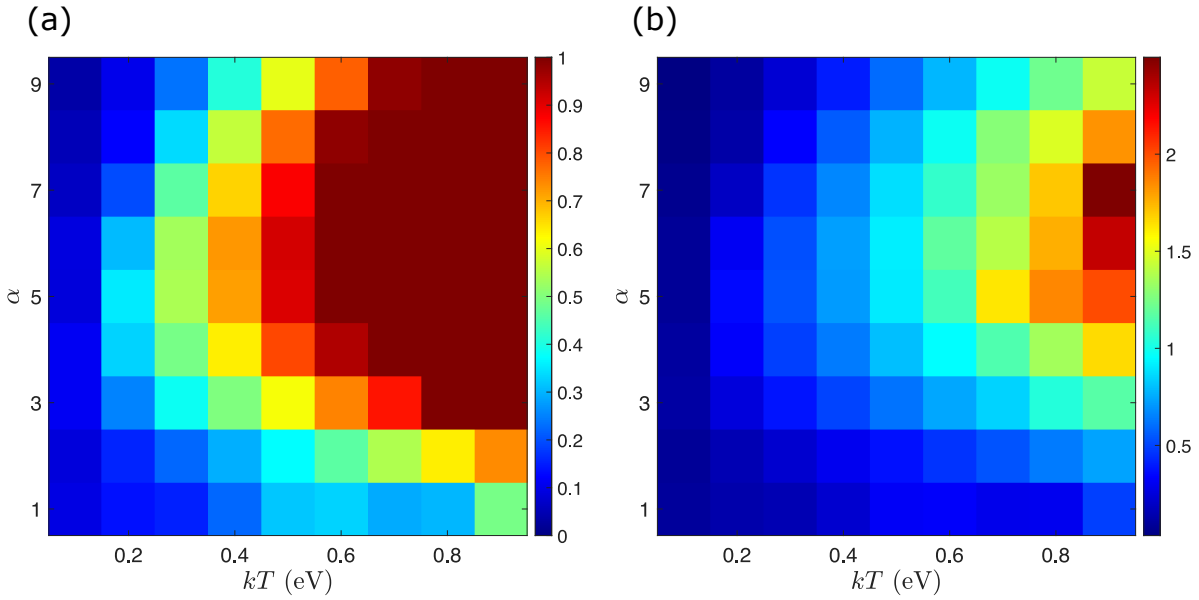

Figure A.1: The value of order parameter ϕ as a function of temperature and aspect ratio α for $L_0 = 30a$ on (a) the same colorbar scale as Fig. 2 in the main text and (b) a colorbar scaled to data.

We also plot the interpolated profile of the membrane, and the profile of the two short free edges with green crosses and triangles and the parallel middle line with grey circle for a variety of parameter sets in Fig. A.2. For small α, we see that the slopes of the top and bottom free edges and that of the middle line are similar at large x. As α gets bigger, the top and bottom edges are steeper than the middle line at large x.

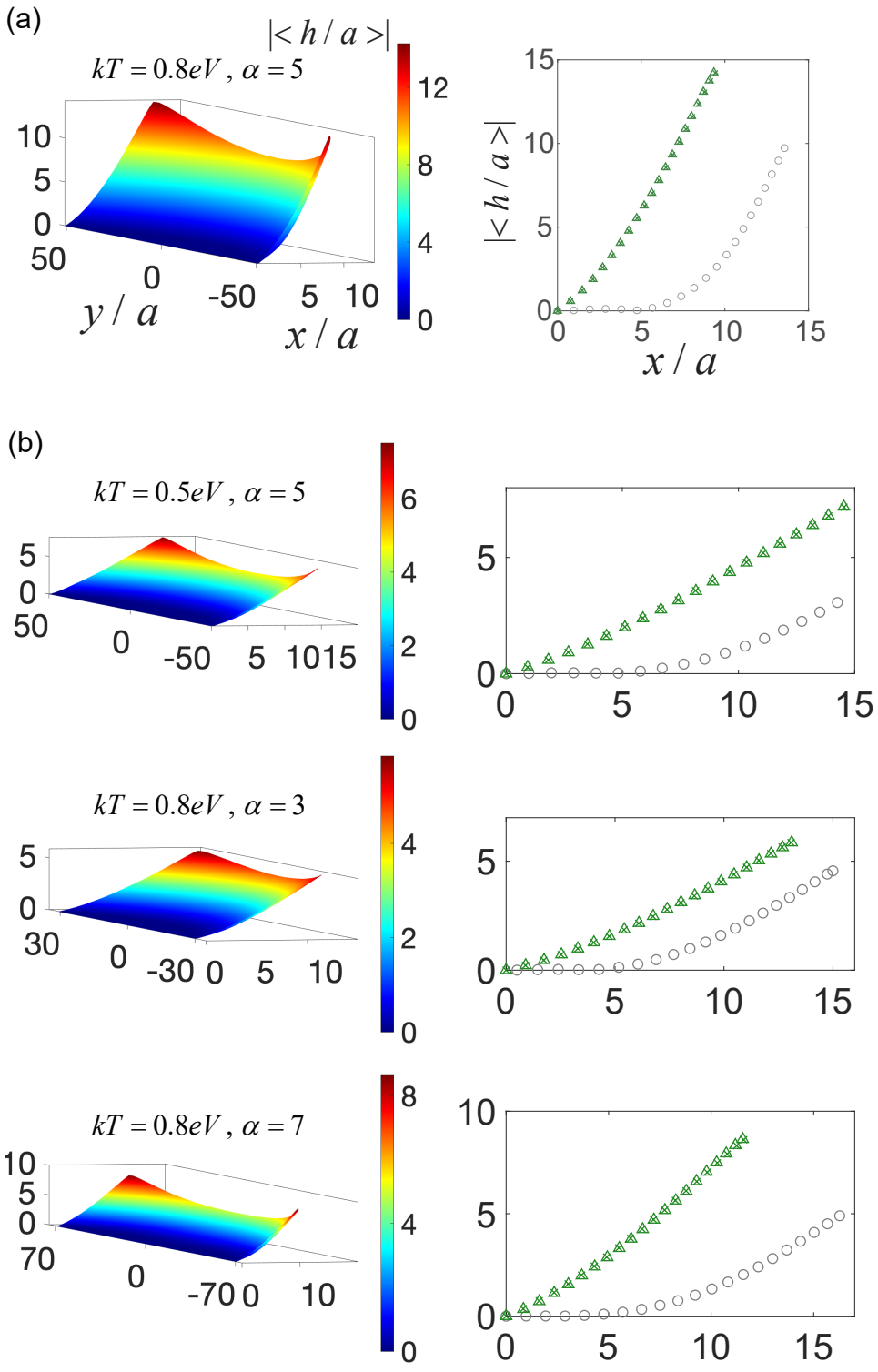

Figure A.2: (a) Reproduction of Fig. 3 in the main text. (b) Configurations for other parameter sets.

A.2 Finite Element Simulations

We perform a finite element (FE) simulation using the FEniCS package [69] to obtain the distribution of the in-plane stress fields in the pre-buckled planar configuration. We minimize the energy functional

$$E = \int d^2x \left[\mu u_{ij}^2 + \frac{1}{2} \lambda u_{kk}^2 \right], \tag{A.3}$$

subject to the boundary conditions $u_x(0, y) = 0$ and $u_y(0, y) = \epsilon y$, for a rectangular sheet on $0 \leq x \leq L$ and $-W/2 \leq y \leq W/2$ [1]. The aspect ratio is $\alpha = W/L$. The boundary condition on u_y represents a uniform stretching of the left edge if $\epsilon > 0$. We measure all stress fields in units of the Young's modulus, which is set to unity in the calculation. Similarly, length is measured in L, which is set to unity. To model a thermalized thin sheet, we choose a negative Poisson ratio of $-1/3$ unless specified otherwise. This is the theoretically predicted Poisson's ratio for a free standing thermalized membrane in the infinite sized limit, which we choose for convenience. Other choices of negative Poisson ratio, or even positive values, make quantitative but not qualitative difference in the in-plane stress fields.

Here we present example results for $\epsilon = 0.05$. The stress fields for $\alpha = 2$ are shown in the top row of Fig. A.3. We see that at this aspect ratio, σ_{xx} has a single compressive region in the middle and two tensile regions in the top and bottom left corners. In comparison, the stress fields at a higher aspect ratio $\alpha = 5$ is shown in the top row of Fig. A.4. In this case, the compressive region breaks down into two, akin to previous results in [64, 66] which study wrinkling in stretched thin films. We expect this is the reason why the system re-enters the horizontal phase at high aspect ratio. This feature of σ_{xx} is also captured qualitatively by our theoretical calculation, as shown below.

[1] L and W here serve the purpose of L' and W' in Chapter 2.

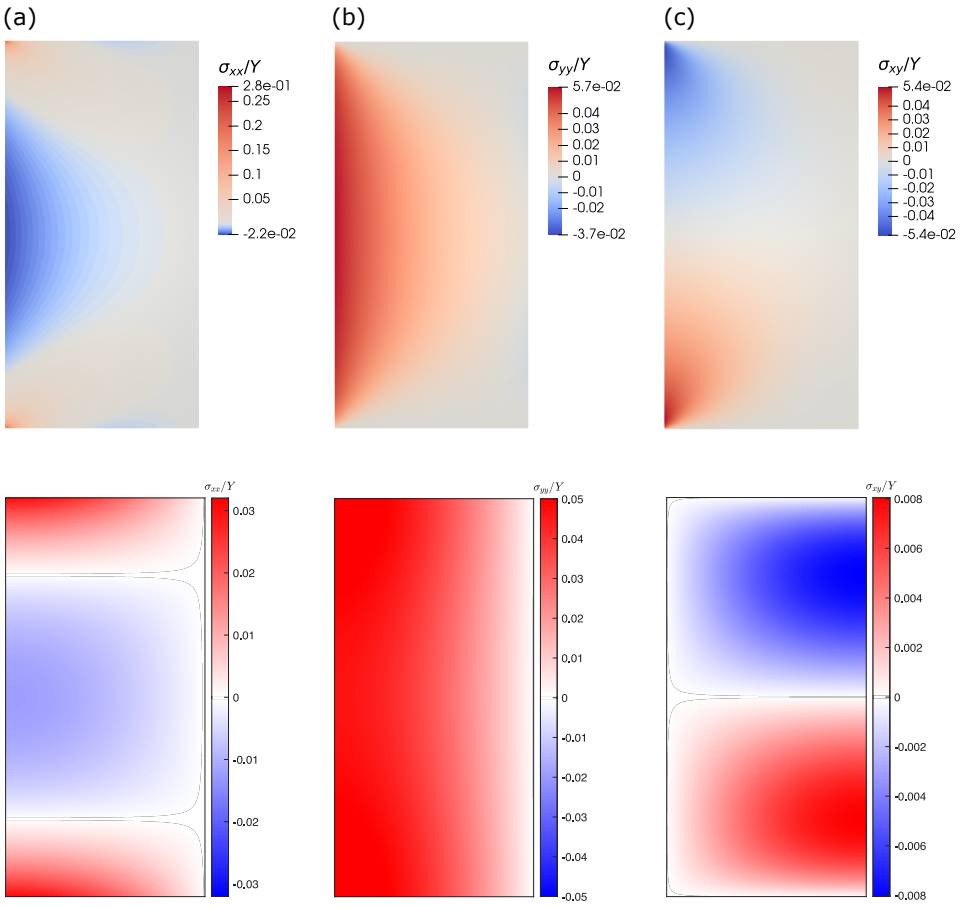

Figure A.3: In-plane stress fields for (a) σ_{xx}/Y, (b) σ_{yy}/Y and (c) σ_{xy}/Y from FEniCS calculation (top row) and theory (bottom row, only half of the doubled system shown). Aspect ratio $\alpha = 2$.

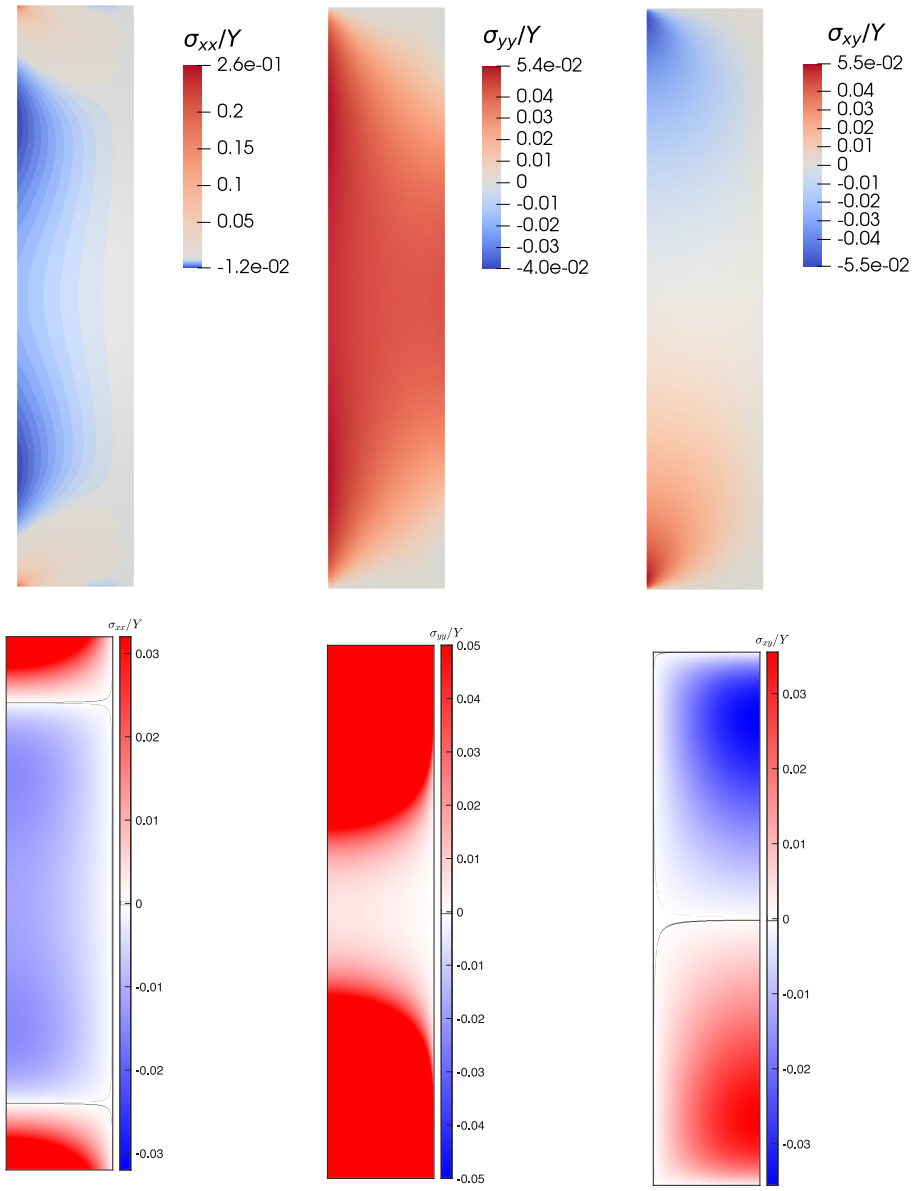

Figure A.4: In-plane stress fields for (a) σ_{xx}/Y, (b) σ_{yy}/Y and (c) σ_{xy}/Y from FEniCS calculation (top row) and theory (bottom row, only half of the doubled system shown). Aspect ratio $\alpha = 5$.

A.3 Analytical Calculations of In-plane Stress Fields

Taking the Hookean approximation and suppressing any out of plane displacement, the in-plane stress fields satisfy [14]

$$\partial_i \sigma_{ij} = 0. \tag{A.4}$$

To solve this 2D elasticity problem with the Airy stress function technique, boundary conditions on all sides in terms of stresses are needed. The stress σ_{xx} due to clamping at $x = 0$ is, however, unknown. Rather, the boundary condition at $x = 0$ is given in terms of the displacement field – Eq. (2.3) in Chapter 2 and $u_x(0, y) = 0$. A way around this issue is to double the original system to the region $-L' \leq x \leq L'$ and $-W'/2 \leq y \leq W'/2$ by reflecting it along the y axis (see Fig. A.5). In the doubled system, we no longer need to provide any condition at $x = 0$ as it is now an internal edge. The condition $u_x(x = 0, y) = 0$ is satisfied automatically.

We introduce the Airy stress function χ, such that $\sigma_{xx} = \chi_{,yy}$, $\sigma_{yy} = \chi_{,xx}$, and $\sigma_{xy} = -\chi_{,xy}$, where the subscripts denote differentiation. Eq. (A.4) implies that χ is biharmonic:

$$\Delta^2 \chi = 0. \tag{A.5}$$

The most general solution involves an infinite series of products in trigonometric and hyperbolic functions in both x and y. To gain analytic tractability, we approximate the boundary conditions in two ways. First, instead of imposing a delta function localized at $x = 0$ for σ_{yy} due to clamping, we impose a delocalized boundary condition $\sigma_{yy}(x, \pm W'/2) = f \cos(\lambda x)$ on the top and bottom edges, where $\lambda = \pi/2L'$. Here f is a force density to be determined self-consistently. Second, we only demand the weak boundary condition $\int \sigma_{xy}(\pm L', y) dy = 0$ on the left and right edges, instead of

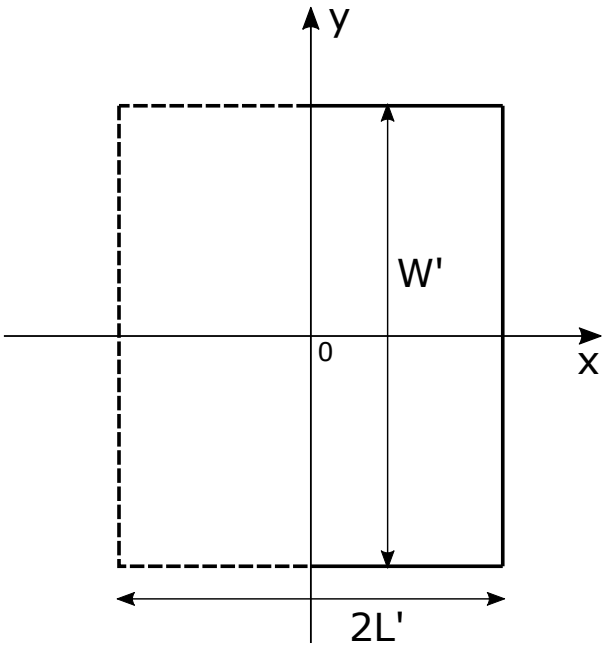

Figure A.5: The doubled system. The original elastic sheet in $x \geq 0$ is doubled by reflection about the y axis.

the strong traction-free condition $\sigma_{xy} = 0$. The remaining boundary conditions are $\sigma_{xx}(x = \pm L', y) = 0$ and $\sigma_{xy}(x, y = \pm W'/2) = 0$. Eq.(A.4) can now be solved with the simple ansatz

$$\chi = [A\cosh(\lambda y) + B\, y \sinh(\lambda y)]\cos(\lambda x), \tag{A.6}$$

which is an even function in both x and y, since σ_{xx} and σ_{yy} should be even in both directions. If we keep more than one Fourier component in $\sigma_{yy}(x, \pm W'/2)$, then χ will be a summation of similar functions with $A \to A_n$, $B \to B_n$, and $\lambda \to \lambda_n$. The stress fields are given by:

$$\begin{aligned}
\sigma_{xx} &= \chi_{,yy} = \left[(A\lambda^2 + 2B\lambda)\cosh(\lambda y) + B\lambda^2 y \sinh(\lambda y)\right]\cos(\lambda x) \\
\sigma_{yy} &= \chi_{,xx} = (-\lambda^2)\left[A\cosh(\lambda y) + B\, y \sinh(\lambda y)\right]\cos(\lambda x) \\
\sigma_{xy} &= -\chi_{,xy} = [B\lambda y \cosh(\lambda y) + (A\lambda + B)\sinh(\lambda y)]\,\lambda \sin(\lambda x).
\end{aligned} \tag{A.7}$$

Note that due to the choice of an anti-periodic Fourier series, $\sigma_{xx}(x = \pm L', y) = 0$ on the left and right edges is automatically satisfied by the ansatz. The weak boundary condition on σ_{xy} on the left and right edges is also satisfied by symmetry. The two unknowns A and B can be solved using the two boundary conditions on the top and bottom edges $\sigma_{xy}(x, y = W'/2) = 0$ and $\sigma_{yy}(x, \pm W'/2) = f\cos(\lambda x)$. The result is given by

$$\begin{aligned}
\sigma_{xx} =& \frac{f}{D}\Big\{[\sinh(\pi\alpha/4) - (\pi\alpha/4)\cosh(\pi\alpha/4)]\cosh(\pi y/2L') \\
&+\frac{\pi}{2L'}\sinh(\pi\alpha/4)\, y \sinh(\pi y/2L')\Big\}\cos(\pi x/2L') \\
\sigma_{yy} =& \frac{f}{D}\Big\{[(\pi\alpha/4)\cosh(\pi\alpha/4) + \sinh(\pi\alpha/4)]\cosh(\pi y/2L') \\
&-\frac{\pi}{2L'}\sinh(\pi\alpha/4)\, y \sinh(\pi y/2L')\Big\}\cos(\pi x/2L') \\
\sigma_{xy} =& \frac{f}{D}\big[\frac{\pi}{2L'}\sinh(\pi\alpha/4)\, y \cosh(\pi y/2L') \\
&-(\pi\alpha/4)\cosh(\pi\alpha/4)\sinh(\pi y/2L')\big]\sin(\pi x/2L'),
\end{aligned} \tag{A.8}$$

where $D = \lambda W'/2 + \cosh(W'\lambda/2)\sinh(W'\lambda/2)$ is a constant, and we have used the aspect ratio $\alpha \equiv W'/L' = W_0/L_0$. We now determine f with the condition

$$u_y(0, \frac{W'}{2}) = -u_y(0, -\frac{W'}{2}) = \frac{W_0 - W'}{2} \equiv \frac{\epsilon}{2}W_0. \tag{A.9}$$

Applying the stress strain relation $u_{yy} = \frac{1}{Y_R}(\sigma_{yy} - \nu_R\sigma_{xx})$ at $x = 0$, we integrate the strain to obtain displacement, resulting in

$$\frac{f}{D} = \frac{\epsilon\pi W_0 Y_R}{8L'\sinh^2(\pi\alpha/4)}, \tag{A.10}$$

which completes our calculation of the in-plane stress. Similarly, applying $u_{xx} = \frac{1}{Y_R}(\sigma_{xx} - \nu_R\sigma_{yy})$ at $y = 0$ and integrating u_{xx}, we obtain the compression of the middle strip given by Eq. (2.5).

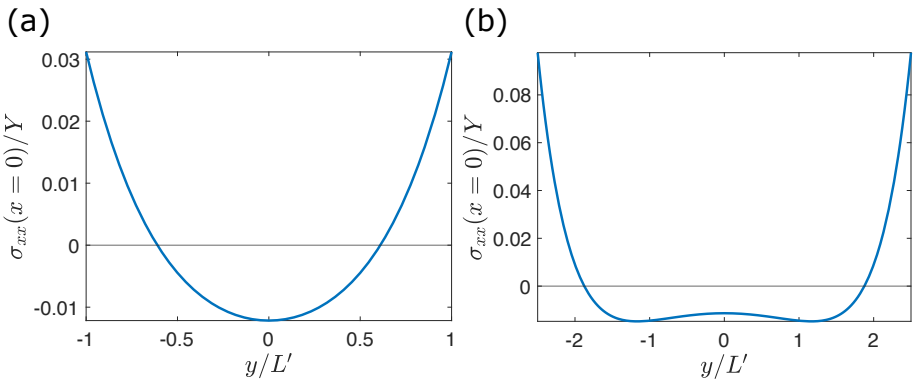

Figure A.6: Theoretical estimation of σ_{xx} at the clamped edge ($x = 0$) for (a) $\alpha = 2$ and (b) $\alpha = 5$. In both cases, $\sigma_{xx} < 0$ in the middle and $\sigma_{xx} > 0$ toward the top and bottom edges.

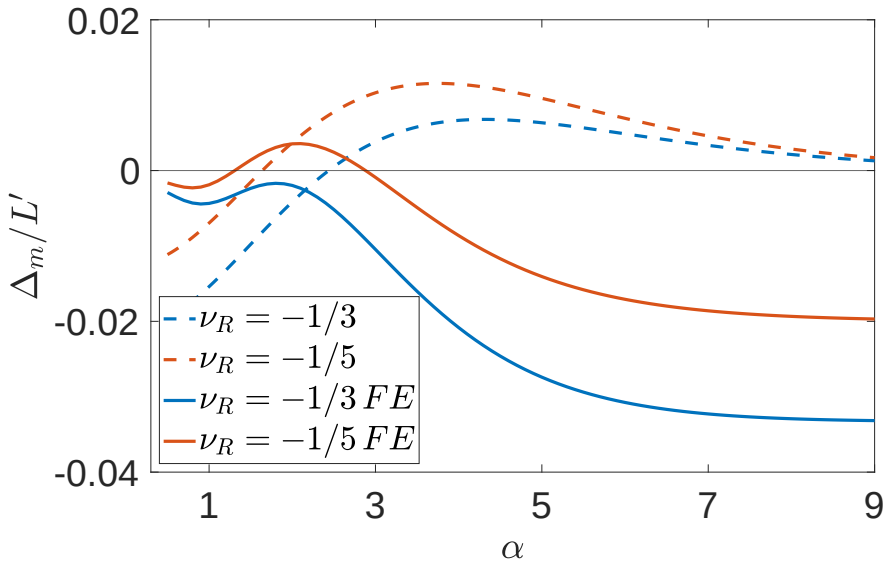

Figure A.7: Compression of the middle strip from finite element calculations with FEniCS (solid curves) and theory (dotted curves).

Fig. A.6 shows σ_{xx} at the clamped edge at $x = 0$. One sees that $\sigma_{xx}(x = 0)$ is negative at $y = 0$ and positive near the top or bottom edge. At high aspect ratio, the compressive region breaks into two, similar to the result from FEniCS calculation. However, there are a few key differences between the finite element calculation, the theoretical calculation and the MD simulation. As seen from Fig. A.3 and Fig. A.4, σ_{xy} obtains its biggest value on the left edge in the finite element calculation, as expected. However, the weak boundary condition we impose and the ansatz we use that allow for a simple analytical calculation leads to a solution where σ_{xy} obtains its biggest value on the right edge. In our estimate for the condition for tilting, we only use the value of stress fields at $y = 0$, on which $\sigma_{xy} = 0$ for both calculations. Since one of the equation is $\partial_x\sigma_{xy} + \partial_y\sigma_{yy} = 0$, the flipped sign in $\partial_x\sigma_{xy}$ leads to a flipped sign in $\partial_y\sigma_{yy}$ in our theoretical result, as seen in Fig. A.4. For a negative Poisson ratio, the tensile σ_{yy} extends the middle strip. Hence the underestimation of σ_{yy} at $y = 0$ leads to an overestimation of the compression of the middle strip, which leads to an overestimation of the tilted phase. We compare the compression of the middle strip from finite element calculations and the theoretical calculation (Fig. 4 in the main text) in Fig. A.7. For finite element calculations, we see that for a Poisson ratio of $-1/3$, the negative Poisson effect is too strong for the compressive σ_{xx} to overcome. The most negative Poisson ratio where we still observe $\Delta_m > 0$ is between $-1/3$ and $-1/4$. The approximations made to obtain the analytical solution can be a main source of the discrepancy between the two methods. But despite the discrepancy, the same feature of the curves, i.e., as the aspect ratio increases the compression increases to a maximal value then decreases, is in agreement with the MD observations that the tilted phase only happens for a finite window of the aspect ratio value.

Examining the optimal aspect ratio where the middle strip is the most compressed reveals a difference between the MD simulation and theoretical and finite element calcu-

lations. In the theoretical calculation, the optimal aspect ratio is about 4, regardless of system size, and it is between 2 and 3 as shown in Fig. A.7 in the finite element calculation. In contrast, the optimal aspect ratio in MD simulations is bigger and seems to have a slight system size dependence, as shown in Fig. 2.2 and Fig. A.1. This suggests that even though we give a qualitative picture for the tilted phase from the perspective of buckling, while ignoring all thermal effects except renormalization of elastic moduli, there are non-trivial thermal effects beyond our simple mean field treatment.

A.4 Effective 1D Theory of Middle Strip

We now derive the effective 1D energy density presented in the main text. For notational simplicity, we drop all subscripts in the elastic moduli, with the assumption that they are all renormalized. We drop the prime in L' so that here $-L \leq x \leq L$. The factors of k_BT in the following calculations are also implied. To restore k_BT and proper dimension, one can replace very $\mathcal{E}$ with $\mathcal{E}/k_BT$. Starting from the full 2D energy in Eq. (2.2) in the main text, we drop the y derivative and u_y to obtain an energy density (per width) functional

$$\begin{aligned}\mathcal{E}[u_x, h] &= \frac{\kappa}{2}\int dx \left(\frac{d^2h}{dx^2}\right)^2 + \frac{Y}{2(1-\nu^2)}\int dx \left[\frac{du_x}{dx} + \frac{1}{2}\left(\frac{dh}{dx}\right)^2\right]^2 \\ &\equiv \mathcal{E}_b[h] + \mathcal{E}_s[u_x, h],\end{aligned} \tag{A.11}$$

where we have used the identity $2\mu+\lambda = \frac{Y}{1-\nu^2}$. u_x is an odd function of x and satisfies the anti-periodic boundary condition $u_x(-L) = -u_x(L) = \Delta/2$. Following the established method (see e.g., Ref. [15]), we define

$$A(x) \equiv \frac{1}{2}\left(\frac{dh}{dx}\right)^2. \tag{A.12}$$

To integrate out u_x and obtain an effective energy density for h only, we perform the Fourier series expansion for anti-periodic functions

$$\begin{aligned} u_x(x) &= \sum_{n=1} \sin(\lambda_n x) u_n \\ A(x) &= \sum_{n=1} \cos(\lambda_n x) A_n, \end{aligned} \tag{A.13}$$

where $\lambda_n = \frac{(2n-1)\pi}{2L}$, and the expansion of $A(x)$ only converges on the open interval $(-L, L)$ since $A(x)$ is an even function with non-zero values on the boundaries. The boundary condition on u_x is equivalent to

$$\sum_{n=1} (-1)^{n-1} u_n = -\Delta/2. \tag{A.14}$$

The second term in Eq. (A.11) in Fourier modes is given by:

$$\mathcal{E}_s[u_x, h] = \frac{YL}{2(1-\nu^2)} \sum_{n=1} (\lambda_n u_n + A_n)^2. \tag{A.15}$$

Formally, the effective density energy is then $\mathcal{E}_{eff}[h] = \mathcal{E}_b - \log\left[\int Du_x e^{-\mathcal{E}_s}\right]$, with the appropriate boundary condition. We impose the boundary condition in the functional integral explicitly by introducing a delta function:

$$\begin{aligned} \mathcal{E}_{eff}[h] &= \mathcal{E}_b - \log\left[\int Du_x e^{-\mathcal{E}_s}\right] \\ &= \mathcal{E}_b - \log\left[\int Du_x\, \delta\left[u_x(L) + \Delta/2\right] e^{-\mathcal{E}_s}\right] \\ &= \mathcal{E}_b - \log\left[\int Du_x \int d\lambda\, e^{i\lambda[u_x(L)+\Delta/2]-\mathcal{E}_s}\right] \\ &= \mathcal{E}_b - \log\left[\int d\lambda \int Du_x\, e^{i\lambda\left[\sum_{n=1}(-1)^{n-1}u_n + \Delta/2\right]-\mathcal{E}_s}\right]. \end{aligned} \tag{A.16}$$

The functional integral over u_x can be calculated in a straightforward way after a change of variable $\lambda_n u_n + A_n \to u_n$. Performing the remaining integral with respect to λ results in:

$$\mathcal{E}_{eff}[h] = \mathcal{E}_b + \frac{Y}{L(1-\nu^2)} \left(\frac{\Delta}{2} + \sum_{n=1} (-1)^n \frac{A_n}{\lambda_n} \right)^2 . \tag{A.17}$$

Substituting

$$A_n = \frac{1}{L} \int dx \, \frac{1}{2} \left(\frac{dh}{dx} \right)^2 \cos(\lambda_n x), \tag{A.18}$$

we observe that the above equation contains the Fourier series of a square-wave function. On the interval of interest $-L \leq x \leq L$, we have:

$$\mathcal{E}_{eff}[h] = \frac{\kappa}{2} \int dx \left(\frac{d^2 h}{dx^2} \right)^2 + \frac{Y}{4L(1-\nu^2)} \left[\Delta - \frac{1}{2} \int dx \left(\frac{dh}{dx} \right)^2 \right]^2 . \tag{A.19}$$

$\mathcal{E}_{eff}$ is then an effective energy density as a function of only h. The last line of Eq. (2.7) presented in Chapter 2 is then obtained by dropping a constant term independent of h.

The derivation above is based on an expansion of $u_x(x)$ with anti-periodic Fourier series. However, it is conventionally more convenient to derive the effective model based on a Fourier expansion of strain, which we present now. Expanding the periodic and even function of strain with the usual Fourier series:

$$\frac{du_x}{dx} = \frac{-\Delta}{2L} + \sum_{n=1} u_n \cos(\frac{n\pi x}{L}). \tag{A.20}$$

Likewise, we expand $A(x)$ with periodic Fourier series

$$A(x) = A_0 + \sum_{n=1} A_n \cos(\frac{n\pi x}{L}), \tag{A.21}$$

where

$$A_0 = \frac{1}{2L}\int \frac{1}{2}\left(\frac{dh}{dx}\right)^2. \tag{A.22}$$

The total energy density takes the form

$$\begin{aligned}\mathcal{E} =&\mathcal{E}_b + \frac{Y}{2(1-\nu^2)}\int\Big[(\frac{-\Delta}{2L}+A_0)+\sum_{n=1}(u_n+A_n)\cos(\frac{n\pi x}{L})\Big]^2\\ =&\mathcal{E}_b + \frac{Y}{2(1-\nu^2)}\Big[2L(\frac{-\Delta}{2L}+A_0)^2+L\sum_{n=1}(u_n+A_n)^2\Big].\end{aligned} \tag{A.23}$$

The second term in the square bracket is quadratic in u_n and can be trivially integrated out, resulting in the effective energy density

$$\begin{aligned}\mathcal{E}_{eff} =&\mathcal{E}_b + \frac{Y}{2(1-\nu^2)}2L\Big[\frac{-\Delta}{2L}+\frac{1}{2L}\int\frac{1}{2}\left(\frac{dh}{dx}\right)^2\Big]^2\\ =&\mathcal{E}_b + \frac{Y}{4L(1-\nu^2)}\left[\Delta-\frac{1}{2}\int dx\left(\frac{dh}{dx}\right)^2\right]^2,\end{aligned} \tag{A.24}$$

which is identical to the result from the previous derivation.

Appendix B

Supplemental Material for Chapter 3

B.1 Triangular Lattices

To describe particles on two-dimensional lattices, we begin by establishing some notations. We label each unit cell with a two-component index $l = (l_1, l_2)$, where l_1 and l_2 are integers. For both triangular and honeycomb lattices, the two primitive lattice vectors are:

$$\mathbf{e}_1 = \begin{pmatrix} 1 \\ 0 \end{pmatrix} \quad \mathbf{e}_2 = \begin{pmatrix} 1/2 \\ \sqrt{3}/2 \end{pmatrix}. \tag{B.1}$$

We also define $\mathbf{e}_3 = \mathbf{e}_2 - \mathbf{e}_1$ for convenience. In a triangular lattice, there is one particle per unit cell, and the equilibrium position of the particle on unit cell l is given by $\mathbf{x}_l = a(l_1\mathbf{e}_1 + l_2\mathbf{e}_2)$, where a is the rest length of the spring, which we set to be $a = 1$ in the following. The position of this particle upon distortion of the lattice is denoted by $\mathbf{r}_l$. The displacement vector of this particle is defined as $\mathbf{u}_l = \mathbf{r}_l - \mathbf{x}_l$. In the lattice basis, Eq. (3.5) becomes:

$$\mathbf{F}_l = -\sum_{l'} \mathbf{D}_{l,l'} \cdot \mathbf{u}_{l'}, \tag{B.2}$$

where $\mathbf{D}_{l,l'}$ is a 2 by 2 matrix for each pair of l and l'.

To find $\mathbf{D}_{l,l'}$, we need to linearize the force law in Eq. (3.1). Consider the spring connecting particle l with one of its nearest-neighbors l'. The distorted spring has length $|\boldsymbol{\Delta}\mathbf{r}| = |\mathbf{r}_l - \mathbf{r}_{l'}| = |\mathbf{x}_l - \mathbf{x}_{l'} + \mathbf{u}_l - \mathbf{u}_{l'}|$. Assuming that the difference between $\mathbf{u}_l$ and $\mathbf{u}_{l'}$ is much smaller than the lattice spacing, we have $\boldsymbol{\Delta}\mathbf{r}/|\boldsymbol{\Delta}\mathbf{r}| \approx \mathbf{e}_{l,l'}$, where $\mathbf{e}_{l,l'} = \mathbf{x}_l - \mathbf{x}_{l'}$ is proportional to one of the unit vectors $\mathbf{e}_i$'s defined previously. The change of length of the spring is approximately $|\boldsymbol{\Delta}\mathbf{r}| - 1 \approx (\mathbf{u}_l - \mathbf{u}_{l'}) \cdot \mathbf{e}_{l,l'}$. Under these approximations, the total force on particle l is given by:

$$\mathbf{F}_l = -{\sum_{l'}}' (k\,\mathbf{e}_{l,l'} + k^o\,\mathbf{e}^*_{l,l'})(\mathbf{u}_l - \mathbf{u}_{l'}) \cdot \mathbf{e}_{l,l'}, \tag{B.3}$$

where the primed sum is over all 6 nearest-neighbors of particle l, and $\mathbf{D}_{l,l'}$ may be read off from this expression. For EMT, however, it is more convenient to cast Eq. (B.2) in the Fourier basis, using periodic boundary condition. Similar to Ref. [79], we use the following lattice Fourier convention for vector quantities:

$$\begin{aligned} \mathbf{u}_l &= \frac{1}{N} \sum_{\mathbf{q}} \mathbf{u}_{\mathbf{q}}\, e^{i\mathbf{q}\cdot\mathbf{x}_l} \\ \mathbf{u}_{\mathbf{q}} &= \sum_{l} \mathbf{u}_l\, e^{-i\mathbf{q}\cdot\mathbf{x}_l}, \end{aligned} \tag{B.4}$$

where N is the number of unit cells in the system, and $\mathbf{q}$ belongs to the first Brillouin zone. The corresponding Fourier convention for matrices is:

$$\begin{aligned} \mathbf{D}_{l,l'} &= \frac{1}{N^2} \sum_{\mathbf{q},\mathbf{q}'} e^{i\mathbf{q}\cdot\mathbf{x}_l}\, \mathbf{D}_{\mathbf{q},\mathbf{q}'}\, e^{-i\mathbf{q}'\cdot\mathbf{x}_{l'}} \\ \mathbf{D}_{\mathbf{q},\mathbf{q}'} &= \sum_{l,l'} e^{-i\mathbf{q}\cdot\mathbf{x}_l}\, \mathbf{D}_{l,l'}\, e^{i\mathbf{q}'\cdot\mathbf{x}_{l'}}. \end{aligned} \tag{B.5}$$

Fourier transforming Eq.(B.2), we obtain:

$$\mathbf{F}_{\mathbf{q}} = -\frac{1}{N}\sum_{\mathbf{q}'} \mathbf{D}_{\mathbf{q},\mathbf{q}'} \cdot \mathbf{u}_{\mathbf{q}'}. \tag{B.6}$$

To facilitate calculations, we define the following translation vectors for lattice indices: $t_1 = (1, 0)$, $t_2 = (0, 1)$, and $t_3 = t_2 - t_1 = (-1, 1)$. The Fourier transform of a translated vector field is:

$$\sum_l \mathbf{u}_{l+t_i}\, e^{-i\mathbf{q}\cdot\mathbf{x}_l} = \mathbf{u}_{\mathbf{q}}\, e^{i\mathbf{q}\cdot\mathbf{e}_i}. \tag{B.7}$$

Since the effective medium in EMT is disorder-free, we first derive the form of $\mathbf{D}_{\mathbf{q},\mathbf{q}'}$ for a homogeneous lattice. Fourier transforming Eq.(B.3), we obtain:

$$\begin{aligned}
\mathbf{F}_{\mathbf{q}} &= -\sum_l \sum_{i=1}^{3} \Big[(k\mathbf{e}_i + k^o \mathbf{e}_i^*)(\mathbf{u}_l - \mathbf{u}_{l+t_i}) \cdot \mathbf{e}_i\, e^{-i\mathbf{q}\cdot\mathbf{x}_l} \\
&\qquad\qquad - (k\mathbf{e}_i + k^o \mathbf{e}_i^*)(\mathbf{u}_l - \mathbf{u}_{l-t_i}) \cdot (-\mathbf{e}_i)\, e^{-i\mathbf{q}\cdot\mathbf{x}_l} \Big] \\
&= -\sum_{i=1}^{3} \Big[(k\mathbf{e}_i + k^o \mathbf{e}_i^*)\, \mathbf{e}_i\, (1 - e^{i\mathbf{q}\cdot\mathbf{e}_i} + 1 - e^{-i\mathbf{q}\cdot\mathbf{e}_i}) \Big] \cdot \mathbf{u}_{\mathbf{q}} \\
&= -\sum_{i=1}^{3} \Big[(k\mathbf{e}_i + k^o \mathbf{e}_i^*)\, \mathbf{e}_i\, (1 - e^{i\mathbf{q}\cdot\mathbf{e}_i})(1 - e^{-i\mathbf{q}\cdot\mathbf{e}_i}) \Big] \cdot \mathbf{u}_{\mathbf{q}} \\
&= -\sum_{i=1}^{3} (k\mathbf{b}_{i,\mathbf{q}}\mathbf{b}_{i,-\mathbf{q}} + k^o \mathbf{b}_{i,\mathbf{q}}^* \mathbf{b}_{i,-\mathbf{q}}) \cdot \mathbf{u}_{\mathbf{q}},
\end{aligned} \tag{B.8}$$

where we define

$$\mathbf{b}_{i,\mathbf{q}} \equiv \mathbf{e}_i(1 - e^{-i\mathbf{q}\cdot\mathbf{e}_i}). \tag{B.9}$$

We note again that when two vectors appear together without a dot in between, they are multiplied in an outer product to form a matrix. Comparing the above equation to

Eq. (B.6), we obtain:

$$\begin{aligned}\mathbf{D}_{\mathbf{q},\mathbf{q}'} &= N\delta_{\mathbf{q},\mathbf{q}'}\sum_{i=1}^{3}(k\mathbf{b}_{i,\mathbf{q}}\mathbf{b}_{i,-\mathbf{q}} + k^o\mathbf{b}^*_{i,\mathbf{q}}\mathbf{b}_{i,-\mathbf{q}}) \\ &\equiv N\delta_{\mathbf{q},\mathbf{q}'}\mathbf{D}_{\mathbf{q}}.\end{aligned} \tag{B.10}$$

For reference, we provide the matrix elements below:

$$\sum_{i=1}^{3}\mathbf{b}_{i,\mathbf{q}}\mathbf{b}_{i,-\mathbf{q}} = \begin{pmatrix} A_{\mathbf{q},xx} & A_{\mathbf{q},xy} \\ A_{\mathbf{q},yx} & A_{\mathbf{q},yy}\end{pmatrix} \tag{B.11}$$

and

$$\sum_{i=1}^{3}\mathbf{b}^*_{i,\mathbf{q}}\mathbf{b}_{i,-\mathbf{q}} = \begin{pmatrix} A_{\mathbf{q},yx} & A_{\mathbf{q},yy} \\ -A_{\mathbf{q},xx} & -A_{\mathbf{q},xy}\end{pmatrix}. \tag{B.12}$$

, where

$$\begin{aligned}A_{\mathbf{q},xx} &= 3 - 2\cos(q_x) - \cos(q_x/2)\cos(\frac{\sqrt{3}}{2}q_y) \\ A_{\mathbf{q},yy} &= 3 - 3\cos(q_x/2)\cos(\frac{\sqrt{3}}{2}q_y) \\ A_{\mathbf{q},xy} &= A_{\mathbf{q},yx} = \sqrt{3}\sin(q_x/2)\sin(\frac{\sqrt{3}}{2}q_y).\end{aligned} \tag{B.13}$$

We also need the dynamical matrix of a single spring for EMT. We choose a spring connecting $l_1 = (0,0)$ and $l_2 = (1,0)$. Since there is only one spring in this setup, $\mathbf{F}_l$ is non-zero only if $l = l_1$ or $l = l_2$. We therefore have the following expression, where repeated l's on the right hand side are *not* summed over:

$$\begin{aligned}\mathbf{F}_l &= -(k\mathbf{e}_1 + k^o\mathbf{e}_1^*)\mathbf{e}_1 \cdot \Big[(\mathbf{u}_l - \mathbf{u}_{l+t_1})\delta_{l,l_1} + (\mathbf{u}_l - \mathbf{u}_{l-t_1})\delta_{l,l_2}\Big] \\ &= \frac{-1}{N}(k\mathbf{e}_1 + k^o\mathbf{e}_1^*)\mathbf{e}_1 \cdot \sum_{\mathbf{q}'}\mathbf{u}_{\mathbf{q}'}e^{i\mathbf{q}'\cdot\mathbf{x}_l}\Big[(1 - e^{i\mathbf{q}'\cdot\mathbf{e}_1})\delta_{l,l_1} + (1 - e^{-i\mathbf{q}'\cdot\mathbf{e}_1})\delta_{l,l_2}\Big].\end{aligned} \tag{B.14}$$

Performing a Fourier tansform, we obtain:

$$\mathbf{F}_{\mathbf{q}} = -\frac{1}{N}\sum_{\mathbf{q}'}(k\mathbf{b}_{1,\mathbf{q}}\mathbf{b}_{1,-\mathbf{q}'} + k^o\mathbf{b}^*_{1,\mathbf{q}}\mathbf{b}_{1,-\mathbf{q}'})\cdot\mathbf{u}_{\mathbf{q}'}. \tag{B.15}$$

The dynamical matrix of a system containing a single spring is therefore:

$$D^{single}_{\mathbf{q},\mathbf{q}'} = k\mathbf{b}_{1,\mathbf{q}}\mathbf{b}_{1,-\mathbf{q}'} + k^o\mathbf{b}^*_{1,\mathbf{q}}\mathbf{b}_{1,-\mathbf{q}'}. \tag{B.16}$$

Compared to the dynamical matrix of a homogeneous lattice in Eq. (B.10), $D^{single}_{\mathbf{q},\mathbf{q}'}$ does not contain a Kronecker delta, and hence couples all pairs of wave vectors $(\mathbf{q},\mathbf{q}')$.

In EMT, the disordered lattice is mapped to a homogeneous, disorder-free effective medium with a dynamical matrix

$$\begin{aligned}\mathbf{D}_{m,\mathbf{q},\mathbf{q}'} &= N\delta_{\mathbf{q},\mathbf{q}'}\sum_{i=1}^{3}(k\mathbf{b}_{i,\mathbf{q}}\mathbf{b}_{i,-\mathbf{q}} + k^o_m\mathbf{b}^*_{i,\mathbf{q}}\mathbf{b}_{i,-\mathbf{q}}) \\ &\equiv N\delta_{\mathbf{q},\mathbf{q}'}\mathbf{D}_{m,\mathbf{q}},\end{aligned} \tag{B.17}$$

where the effective odd spring constant k^o_m is an unknown to be determined self-consistently, and we assume that the passive spring constant k is unaffected by disorder. The Green's function of the effective medium is

$$\begin{aligned}\mathbf{G}_{m,\mathbf{q},\mathbf{q}'} &= -(\mathbf{D}_{m,\mathbf{q},\mathbf{q}'})^{-1} = \frac{1}{N}\delta_{\mathbf{q},\mathbf{q}'}(-\mathbf{D}_{m,\mathbf{q}})^{-1} \\ &\equiv \frac{1}{N}\delta_{\mathbf{q},\mathbf{q}'}\mathbf{G}_{m,\mathbf{q}}.\end{aligned} \tag{B.18}$$

To establish a self-consistent condition, we first replace one of the effective odd springs in the effective medium with an odd spring with odd constant k^o_s. To mimic the random nature of the original setup described in Chapter 3, k^o_s is a random variable which equals k^o with a probability of p and $k^o_s = 0$ with a probability of $1-p$. The passive spring

constant k is unchanged by the replacement, and in the following we set $k = 1$. Without loss of generality, we choose to replace the spring connecting $l_1 = (0, 0)$ and $l_2 = (1, 0)$. The replacement corresponds to a random dynamical matrix:

$$V_{\mathbf{q},\mathbf{q}'} = (k_s^o - k_m^o)\mathbf{b}_{1,\mathbf{q}}^* \mathbf{b}_{1,-\mathbf{q}'}. \tag{B.19}$$

Similar to $D_{\mathbf{q},\mathbf{q}'}^{single}$, $V_{\mathbf{q},\mathbf{q}'}$ couples all pairs of wave vectors. The absence of the factor of N compared to $\mathbf{D}_{m,\mathbf{q},\mathbf{q}'}$ allows us to treat it as a perturbation to the latter. In the following derivation, we omit writing the $(\mathbf{q}, \mathbf{q}')$ subscripts. The perturbed dynamical matrix is $\mathbf{D}' = \mathbf{D}_m + \mathbf{V}$, and the perturbed Green's function is:

$$\begin{aligned}
\mathbf{G}' &= -(\mathbf{D}')^{-1} = [(\mathbf{G}_m)^{-1} - \mathbf{V}]^{-1} = \mathbf{G}_m \cdot (\mathbf{I} - \mathbf{V} \cdot \mathbf{G}_m)^{-1} \\
&= \mathbf{G}_m \cdot (\mathbf{I} + \mathbf{V} \cdot \mathbf{G}_m + \mathbf{V} \cdot \mathbf{G}_m \cdot \mathbf{V} \cdot \mathbf{G}_m + ...) \\
&= \mathbf{G}_m + \mathbf{G}_m \cdot \mathbf{T} \cdot \mathbf{G}_m,
\end{aligned} \tag{B.20}$$

where the series expansion is allowed because $\mathbf{V} \cdot \mathbf{G}_m \sim (1/N)$. The T-matrix is

$$\mathbf{T} = \mathbf{V} + \mathbf{V} \cdot \mathbf{G}_m \cdot \mathbf{V} + \mathbf{V} \cdot \mathbf{G}_m \cdot \mathbf{V} \cdot \mathbf{G}_m \cdot \mathbf{V} + ... \tag{B.21}$$

Since the effective medium is a faithful representation of the original disordered system, replacing a single spring with a spring drawn from the original disorder probability distribution should, on average, have no impact on the effective medium. We therefore impose $\langle \mathbf{G}' \rangle = \mathbf{G}_m$, which is solved by the equation $\langle \mathbf{T} \rangle = 0$. This equation allows us to solve for the effective odd elastic constant k_m^o, as we show below.

Computing the T-matrix, we obtain:

$$\mathbf{T}_{\mathbf{q},\mathbf{q}'} = T\, \mathbf{b}_{1,\mathbf{q}}^*\, \mathbf{b}_{1,-\mathbf{q}'}, \tag{B.22}$$

where the scalar T reads:

$$T = \frac{k_s^o - k_m^o}{1 - (k_s^o - k_m^o)\sum_{\mathbf{q}} \frac{1}{N} \mathbf{b}_{1,-\mathbf{q}} \cdot \mathbf{G}_{m,\mathbf{q}} \cdot \mathbf{b}_{1,\mathbf{q}}^*}. \tag{B.23}$$

Defining the following function:

$$H(k_m^o) \equiv -k_m^o \sum_{\mathbf{q}} \frac{1}{N} \mathbf{b}_{1,-\mathbf{q}} \cdot \mathbf{G}_{m,\mathbf{q}} \cdot \mathbf{b}_{1,\mathbf{q}}^*, \tag{B.24}$$

we express T in the following form:

$$T = \frac{k_s^o - k_m^o}{1 + (\frac{k_s^o}{k_m^0} - 1) H(k_m^o)}. \tag{B.25}$$

The equation $\langle T \rangle = 0$ then leads to the following equation of k_m^o:

$$k_m^o = k^o \frac{p - H(k_m^o)}{1 - H(k_m^o)}. \tag{B.26}$$

The summation over $\mathbf{q}$ in $H(k_m^o)$ can be computed by taking the continuum ($N \to \infty$) limit and converting the sum to an integral over the first Brillouin zone (see, for example, Appendix 2A of Ref. [89]), resulting in

$$H(k_m^o) = \frac{2}{3} \frac{(k_m^o)^2}{1 + (k_m^o)^2}. \tag{B.27}$$

Eq. (B.26) then reduces to the following cubic equation which gives rise to various results in Chapter 3:

$$(k_m^o)^3 + 3k_m^o = k^o \left[3p + (3p - 2)(k_m^o)^2\right]. \tag{B.28}$$

B.2 Honeycomb Lattices

A honeycomb lattice is a triangular lattice of unit cells, each containing two particles, labelled by A and B. Every particle has three nearest neighbors, one from the same unit cell and the other two from adjacent unit cells. A nearest neighbor spring connects particles of different types, and is in the direction of one of the three unit vectors below:

$$\mathbf{a}_1 = \begin{pmatrix} 0 \\ 1 \end{pmatrix} \quad \mathbf{a}_2 = \begin{pmatrix} -\sqrt{3}/2 \\ -1/2 \end{pmatrix} \quad \mathbf{a}_3 = \begin{pmatrix} \sqrt{3}/2 \\ -1/2 \end{pmatrix}. \tag{B.29}$$

Every particle has 6 next-nearest-neighbors (NNN) of the same type, and the NNN network consists of two overlapping triangular lattices, one for each particle type. We use the length of a NNN spring as the unit of length. In the lattice basis, Eq. (3.5) reads

$$\begin{pmatrix} \mathbf{F}_l^A \\ \mathbf{F}_l^B \end{pmatrix} = -\sum_{l'} \mathbf{D}_{l,l'} \cdot \mathbf{u}_{l'} = -\sum_{l'} \begin{pmatrix} \mathbf{D}_{l,l'}^{AA} & \mathbf{D}_{l,l'}^{AB} \\ \mathbf{D}_{l,l'}^{BA} & \mathbf{D}_{l,l'}^{BB} \end{pmatrix} \cdot \begin{pmatrix} \mathbf{u}_{l'}^A \\ \mathbf{u}_{l'}^B \end{pmatrix}, \tag{B.30}$$

where $\mathbf{F}_l^\alpha$ is the force on the type-α particle on unit cell l, and $\mathbf{D}_{l,l'}^{\alpha\beta}$ is a 2 by 2 matrix for a given pair of (l, l') and (α, β). The 4 by 4 dynamical matrix $\mathbf{D}_{l,l'}$ is the sum of a nearest-neighbor part $\mathbf{D}_{l,l}^{NN}$ and a next-nearest-neighbor part $\mathbf{D}_{l,l}^{NNN}$. The former has the general form:

$$\mathbf{D}_{l,l}^{NN} = \begin{pmatrix} \mathbf{D}_{l,l'}^{NN,AA} & \mathbf{D}_{l,l'}^{NN,AB} \\ \mathbf{D}_{l,l'}^{NN,BA} & \mathbf{D}_{l,l'}^{NN,BB} \end{pmatrix}, \tag{B.31}$$

while the latter is block diagonal

$$\mathbf{D}_{l,l}^{NNN} = \begin{pmatrix} \mathbf{D}_{l,l'}^{NNN,AA} & \mathbf{0} \\ \mathbf{0} & \mathbf{D}_{l,l'}^{NNN,BB} \end{pmatrix}, \tag{B.32}$$

because the two NNN triangular lattices are disjoint.

Similarly, in Fourier space, we have

$$\mathbf{D}_{\mathbf{q},\mathbf{q}'} = \mathbf{D}^{NN}_{\mathbf{q},\mathbf{q}'} + \mathbf{D}^{NNN}_{\mathbf{q},\mathbf{q}'}, \tag{B.33}$$

and the NNN contribution is block diagonal:

$$\mathbf{D}^{NNN}_{\mathbf{q},\mathbf{q}'} = \begin{pmatrix} \mathbf{D}^{NNN,AA}_{\mathbf{q},\mathbf{q}'} & \mathbf{0} \\ \mathbf{0} & \mathbf{D}^{NNN,BB}_{\mathbf{q},\mathbf{q}'} \end{pmatrix}. \tag{B.34}$$

Using Eq. (B.10), we have:

$$\mathbf{D}^{NNN,AA}_{\mathbf{q},\mathbf{q}'} = \mathbf{D}^{NNN,BB}_{\mathbf{q},\mathbf{q}'} = N\delta_{\mathbf{q},\mathbf{q}'} \sum_{i=1}^{3} (k_2 \mathbf{b}_{i,\mathbf{q}} \mathbf{b}_{i,-\mathbf{q}} + k_2^o \mathbf{b}^*_{i,\mathbf{q}} \mathbf{b}_{i,-\mathbf{q}}), \tag{B.35}$$

where k_2 is the passive NNN spring constant, and k_2^o is the odd NNN spring constant. Defining two sets of four-dimensional vectors:

$$\mathbf{c}_{i,\mathbf{q}} = \begin{pmatrix} \mathbf{b}_{i,\mathbf{q}} \\ \mathbf{0} \end{pmatrix} \quad \mathbf{d}_{i,\mathbf{q}} = \begin{pmatrix} \mathbf{0} \\ \mathbf{b}_{i,\mathbf{q}} \end{pmatrix}, \tag{B.36}$$

we can write the 4 by 4 NNN dynamical matrix as:

$$\mathbf{D}^{NNN}_{\mathbf{q},\mathbf{q}'} = N\delta_{\mathbf{q},\mathbf{q}'} \mathbf{D}^{NNN}_{\mathbf{q}}, \tag{B.37}$$

where

$$\mathbf{D}^{NNN}_{\mathbf{q}} = k_2 \sum_{i=1}^{3} (\mathbf{c}_{i,\mathbf{q}} \mathbf{c}_{i,\mathbf{q}} + \mathbf{d}_{i,\mathbf{q}} \mathbf{d}_{i,-\mathbf{q}}) + k_2^o \sum_{i=1}^{3} (\mathbf{c}^*_{i,\mathbf{q}} \mathbf{c}_{i,\mathbf{q}} + \mathbf{d}^*_{i,\mathbf{q}} \mathbf{d}_{i,-\mathbf{q}}). \tag{B.38}$$

For the NN network, in the lattice basis, we have:

$$\begin{aligned}\mathbf{F}_l^A = &- (k_1\mathbf{a}_1 + k_1^o\mathbf{a}_1^*)\cdot(\mathbf{u}_l^A - \mathbf{u}_l^B)\\ &- (k_1\mathbf{a}_2 + k_1^o\mathbf{a}_2^*)\cdot(\mathbf{u}_l^A - \mathbf{u}_{l-t_2}^B)\\ &- (k_1\mathbf{a}_3 + k_1^o\mathbf{a}_3^*)\cdot(\mathbf{u}_l^A - \mathbf{u}_{l-t_3}^B),\end{aligned} \tag{B.39}$$

and

$$\begin{aligned}\mathbf{F}_l^B = &- (k_1\mathbf{a}_1 + k_1^o\mathbf{a}_1^*)\cdot(\mathbf{u}_l^B - \mathbf{u}_l^A)\\ &- (k_1\mathbf{a}_2 + k_1^o\mathbf{a}_2^*)\cdot(\mathbf{u}_l^B - \mathbf{u}_{l+t_2}^A)\\ &- (k_1\mathbf{a}_3 + k_1^o\mathbf{a}_3^*)\cdot(\mathbf{u}_l^B - \mathbf{u}_{l+t_3}^A),\end{aligned} \tag{B.40}$$

where the lattice translation vectors are defined in the paragraph below Eq. (B.6). To simplify the expressions in Fourier space, we define the vectors: $\mathbf{f}_1 = \mathbf{0}$, $\mathbf{f}_2 = \mathbf{e}_2$ and $\mathbf{f}_3 = \mathbf{e}_3$. Fourier transforming Eq. (B.40), we obtain:

$$\mathbf{F}_{\mathbf{q}}^A = -\sum_{i=1}^{3}(k_1\mathbf{a}_i + k_1^o\mathbf{a}_i^*)\mathbf{a}_i\cdot(\mathbf{u}_{\mathbf{q}}^A - \mathbf{u}_{\mathbf{q}}^B\, e^{-i\mathbf{q}\cdot\mathbf{f}_i}), \tag{B.41}$$

and

$$\mathbf{F}_{\mathbf{q}}^B = -\sum_{i=1}^{3}(k_1\mathbf{a}_i + k_1^o\mathbf{a}_i^*)\mathbf{a}_i\cdot(\mathbf{u}_{\mathbf{q}}^B - \mathbf{u}_{\mathbf{q}}^A\, e^{i\mathbf{q}\cdot\mathbf{f}_i}). \tag{B.42}$$

The NN dynamical matrix then reads:

$$\mathbf{D}_{\mathbf{q},\mathbf{q}'}^{NN} = N\delta_{\mathbf{q},\mathbf{q}'}\mathbf{D}_{\mathbf{q}}^{NN}, \tag{B.43}$$

with 2 by 2 block matrices:

$$\mathbf{D}_{\mathbf{q}}^{NN,AA} = \mathbf{D}_{\mathbf{q}}^{NN,BB} = k_1\sum_{i=1}^{3}\mathbf{a}_i\mathbf{a}_i + k_1^o\sum_{i=1}^{3}\mathbf{a}_i^*\mathbf{a}_i \tag{B.44}$$

and

$$\mathbf{D}_{\mathbf{q}}^{NN,AB} = \overline{\mathbf{D}_{\mathbf{q}}^{NN,AB}} = -k_1 \sum_{i=1}^{3} \mathbf{a}_i \mathbf{a}_i \, e^{-i\mathbf{q}\cdot\mathbf{f}_i} - k_1^o \sum_{i=1}^{3} \mathbf{a}_i^* \mathbf{a}_i \, e^{-i\mathbf{q}\cdot\mathbf{f}_i}. \tag{B.45}$$

The long bar denotes complex conjugation in the above equation. For the purpose of EMT, these results can be organized by defining another set of four-dimensional vectors:

$$\mathbf{g}_{i,\mathbf{q}} = \begin{pmatrix} -\mathbf{a}_i \\ \mathbf{a}_i \, e^{i\mathbf{q}\cdot\mathbf{f}_i} \end{pmatrix}. \tag{B.46}$$

Then we have:

$$\mathbf{D}_{\mathbf{q}}^{NN} = k_1 \sum_{i=1}^{3} \mathbf{g}_{i,\mathbf{q}} \mathbf{g}_{i,-\mathbf{q}} + k_1^o \sum_{i=1}^{3} \mathbf{g}_{i,\mathbf{q}}^* \mathbf{g}_{i,-\mathbf{q}}. \tag{B.47}$$

The dynamical matrix of the effective medium is obtained by replacing k_1^o and k_2^o by $k_{1,m}^o$ and $k_{2,m}^o$ in Eq. (B.38) and Eq. (B.47). The perturbation dynamical matrix by replacing a single NN spring is

$$\mathbf{V}_{\mathbf{q},\mathbf{q}'}^{NN} = (k_{1,s}^o - k_{1,m}^o) \mathbf{g}_{1,\mathbf{q}}^* \mathbf{g}_{1,-\mathbf{q}'}, \tag{B.48}$$

and the one for an NNN spring is

$$\mathbf{V}_{\mathbf{q},\mathbf{q}'}^{NNN} = (k_{2,s}^o - k_{2,m}^o) \mathbf{c}_{1,\mathbf{q}}^* \mathbf{c}_{1,-\mathbf{q}'}. \tag{B.49}$$

Similar to the triangular lattice case, the T-matrix for the NN replacement is given by

$$\mathbf{T}_{\mathbf{q},\mathbf{q}'}^{NN} = T^{NN} \mathbf{g}_{1,\mathbf{q}}^* \mathbf{g}_{1,-\mathbf{q}'}, \tag{B.50}$$

where the scalar T^{NN} is given by:

$$T^{NN} = \frac{k^o_{1,s} - k^o_{1,m}}{1 - (k^o_{1,s} - k^o_{1,m}) \sum_{\mathbf{q}} \frac{1}{N} \mathbf{g}_{1,-\mathbf{q}} \cdot \mathbf{G}_{m,\mathbf{q}} \cdot \mathbf{g}^*_{1,\mathbf{q}}}. \tag{B.51}$$

The form of $\mathbf{G}_{m,\mathbf{q}}$ is obtained by inverting the dynamical matrix in Eq. (B.33). The T-matrix for the NNN replacement is given by:

$$\mathbf{T}^{NNN}_{\mathbf{q},\mathbf{q}'} = T^{NNN} \mathbf{c}^*_{1,\mathbf{q}} \mathbf{c}_{1,-\mathbf{q}'}, \tag{B.52}$$

where

$$T^{NNN} = \frac{k^o_{2,s} - k^o_{2,m}}{1 - (k^o_{2,s} - k^o_{2,m}) \sum_{\mathbf{q}} \frac{1}{N} \mathbf{c}_{1,-\mathbf{q}} \cdot \mathbf{G}_{m,\mathbf{q}} \cdot \mathbf{c}^*_{1,\mathbf{q}}}. \tag{B.53}$$

The two functions $H_1(k^o_{1,m}, k^o_{2,m})$ and $H_2(k^o_{1,m}, k^o_{2,m})$ in Chapter 3 are defined as:

$$H_1(k^o_{1,m}, k^o_{2,m}) = -k^o_{1,m} \sum_{\mathbf{q}} \frac{1}{N} \mathbf{g}_{1,-\mathbf{q}} \cdot \mathbf{G}_{m,\mathbf{q}} \cdot \mathbf{g}^*_{1,\mathbf{q}}, \tag{B.54}$$

and

$$H_2(k^o_{1,m}, k^o_{2,m}) = -k^o_{2,m} \sum_{\mathbf{q}} \frac{1}{N} \mathbf{c}_{1,-\mathbf{q}} \cdot \mathbf{G}_{m,\mathbf{q}} \cdot \mathbf{c}^*_{1,\mathbf{q}}. \tag{B.55}$$

The two unknowns $k^o_{1,m}$ and $k^o_{2,m}$ are solved self-consistently by requiring $\langle T_1 \rangle = 0$ and $\langle T_2 \rangle = 0$, resulting in Eq. (3.19) in Chapter 3. Unlike the situation with triangular lattices, we do not find any convenient closed form for H_1 and H_2. Consequently, we rely entirely on numerical methods to solve the EMT equations.

Bibliography

[1] S. Timoshenko, *History of strength of materials: with a brief account of the history of theory of elasticity and theory of structures*. Courier Corporation, 1983.

[2] A. E. H. Love, *A treatise on the mathematical theory of elasticity*. University press, 1927.

[3] L. Euler, *Methodus inveniendi lineas curvas maximi minimive proprietate gaudentes sive solutio problematis isoperimetrici latissimo sensu accepti*, vol. 1. Springer Science & Business Media, 1952.

[4] G. Greenhill, *Determination of the greatest height consistent with stability that a vertical pole or mast can be made, and the greatest height to which a tree of given proportions can grow*, in *Proceedings of the Cambridge Philosophical Society*, vol. 4, p. 65, 1881.

[5] T. Mullin, S. Deschanel, K. Bertoldi, and M. C. Boyce, *Pattern transformation triggered by deformation*, *Physical review letters* **99** (2007), no. 8 084301.

[6] K. Bertoldi, P. M. Reis, S. Willshaw, and T. Mullin, *Negative poisson's ratio behavior induced by an elastic instability*, *Advanced materials* **22** (2010), no. 3 361–366.

[7] K. Bertoldi, V. Vitelli, J. Christensen, and M. Van Hecke, *Flexible mechanical metamaterials*, *Nature Reviews Materials* **2** (2017), no. 11 1–11.

[8] T. J. Byers and D. Branton, *Visualization of the protein associations in the erythrocyte membrane skeleton.*, *Proceedings of the National Academy of Sciences* **82** (1985), no. 18 6153–6157.

[9] D. Nelson, T. Piran, and S. Weinberg, *Statistical mechanics of membranes and surfaces*. World Scientific, 2004.

[10] D. Akinwande, C. J. Brennan, J. S. Bunch, P. Egberts, J. R. Felts, H. Gao, R. Huang, J.-S. Kim, T. Li, Y. Li, *et. al.*, *A review on mechanics and mechanical properties of 2d materials—graphene and beyond*, *Extreme Mechanics Letters* **13** (2017) 42–77.

[11] M. J. Bowick and A. Travesset, *The statistical mechanics of membranes*, *Physics Reports* **344** (2001), no. 4-6 255–308.

[12] G. Salbreux and F. Jülicher, *Mechanics of active surfaces*, *Physical Review E* **96** (2017), no. 3 032404.

[13] C. Scheibner, A. Souslov, D. Banerjee, P. Surówka, W. T. Irvine, and V. Vitelli, *Odd elasticity*, *Nature Physics* **16** (2020), no. 4 475–480.

[14] L. D. Landau, E. M. Lifshitz, A. M. Kosevich, and L. P. Pitaevskii, *Theory of elasticity: volume 7*, vol. 7. Elsevier, 1986.

[15] D. Nelson and L. Peliti, *Fluctuations in membranes with crystalline and hexatic order*, *Journal de physique* **48** (1987), no. 7 1085–1092.

[16] M. I. Katsnelson, *The Physics of Graphene*. Cambridge University Press, 2 ed., 2020.

[17] J. A. Aronovitz and T. C. Lubensky, *Fluctuations of solid membranes*, *Physical review letters* **60** (1988), no. 25 2634.

[18] O. Coquand, D. Mouhanna, and S. Teber, *Flat phase of polymerized membranes at two-loop order*, *Physical Review E* **101** (2020), no. 6 062104.

[19] S. Metayer, D. Mouhanna, and S. Teber, *Three-loop order approach to flat polymerized membranes*, *Physical Review E* **105** (2022), no. 1 L012603.

[20] P. Le Doussal and L. Radzihovsky, *Self-consistent theory of polymerized membranes*, *Physical review letters* **69** (1992), no. 8 1209.

[21] J.-P. Kownacki and D. Mouhanna, *Crumpling transition and flat phase of polymerized phantom membranes*, *Physical Review E* **79** (2009), no. 4 040101.

[22] N. D. Mermin and H. Wagner, *Absence of ferromagnetism or antiferromagnetism in one-or two-dimensional isotropic heisenberg models*, *Physical Review Letters* **17** (1966), no. 22 1133.

[23] D. R. Nelson, *Defects and geometry in condensed matter physics*. Cambridge University Press, 2002.

[24] A. Košmrlj and D. R. Nelson, *Response of thermalized ribbons to pulling and bending*, *Physical Review B* **93** (2016), no. 12 125431.

[25] J. Aronovitz, L. Golubovic, and T. Lubensky, *Fluctuations and lower critical dimensions of crystalline membranes*, *Journal de Physique* **50** (1989), no. 6 609–631.

[26] A. Fasolino, J. Los, and M. I. Katsnelson, *Intrinsic ripples in graphene*, *Nature materials* **6** (2007), no. 11 858–861.

[27] C. Lee, X. Wei, J. W. Kysar, and J. Hone, *Measurement of the elastic properties and intrinsic strength of monolayer graphene*, *science* **321** (2008), no. 5887 385–388.

[28] H. Zhao, K. Min, and N. R. Aluru, *Size and chirality dependent elastic properties of graphene nanoribbons under uniaxial tension*, *Nano letters* **9** (2009), no. 8 3012–3015.

[29] M. K. Blees, A. W. Barnard, P. A. Rose, S. P. Roberts, K. L. McGill, P. Y. Huang, A. R. Ruyack, J. W. Kevek, B. Kobrin, D. A. Muller, *et. al.*, *Graphene kirigami*, *Nature* **524** (2015), no. 7564 204–207.

[30] P. Le Doussal and L. Radzihovsky, *Anomalous elasticity, fluctuations and disorder in elastic membranes*, *Annals of Physics* **392** (2018) 340–410.

[31] R. J. Nicholl, H. J. Conley, N. V. Lavrik, I. Vlassiouk, Y. S. Puzyrev, V. P. Sreenivas, S. T. Pantelides, and K. I. Bolotin, *The effect of intrinsic crumpling on the mechanics of free-standing graphene*, *Nature communications* **6** (2015), no. 1 8789.

[32] Z. Chen, D. Wan, and M. J. Bowick, *Spontaneous tilt of single-clamped thermal elastic sheets*, *Physical Review Letters* **128** (2022), no. 2 028006.

[33] M. C. Marchetti, J.-F. Joanny, S. Ramaswamy, T. B. Liverpool, J. Prost, M. Rao, and R. A. Simha, *Hydrodynamics of soft active matter*, *Reviews of modern physics* **85** (2013), no. 3 1143.

[34] M. J. Bowick, N. Fakhri, M. C. Marchetti, and S. Ramaswamy, *Symmetry, thermodynamics, and topology in active matter*, *Physical Review X* **12** (2022), no. 1 010501.

[35] T. Lecuit and P.-F. Lenne, *Cell surface mechanics and the control of cell shape, tissue patterns and morphogenesis*, *Nature reviews Molecular cell biology* **8** (2007), no. 8 633–644.

[36] M. Fossati, C. Scheibner, M. Fruchart, and V. Vitelli, *Odd elasticity and topological waves in active surfaces*, *arXiv preprint arXiv:2210.03669* (2022).

[37] M. Fruchart, C. Scheibner, and V. Vitelli, *Odd viscosity and odd elasticity*, *Annual Review of Condensed Matter Physics* **14** (2023) 471–510.

[38] X. Mao and T. C. Lubensky, *Maxwell lattices and topological mechanics*, *Annual Review of Condensed Matter Physics* **9** (2018) 413–433.

[39] M. Born and K. Huang, *Dynamical theory of crystal lattices*. Oxford university press, 1996.

[40] L. Braverman, C. Scheibner, B. VanSaders, and V. Vitelli, *Topological defects in solids with odd elasticity*, *Physical Review Letters* **127** (2021), no. 26 268001.

[41] A. Poncet and D. Bartolo, *When soft crystals defy newton's third law: Nonreciprocal mechanics and dislocation motility*, *Physical Review Letters* **128** (2022), no. 4 048002.

[42] Z. Chen, *Odd moduli of disordered odd elastic lattices*, *arXiv preprint arXiv:2204.06587* (2022).

[43] E. R. Russell, R. Sknepnek, and M. Bowick, *Stiffening thermal membranes by cutting*, *Physical Review E* **96** (2017), no. 1 013002.

[44] D. Yllanes, S. S. Bhabesh, D. R. Nelson, and M. J. Bowick, *Thermal crumpling of perforated two-dimensional sheets*, *Nature communications* **8** (2017), no. 1 1381.

[45] K. Ekinci and M. Roukes, *Nanoelectromechanical systems*, *Review of scientific instruments* **76** (2005), no. 6.

[46] A. Košmrlj and D. R. Nelson, *Statistical mechanics of thin spherical shells*, *Physical Review X* **7** (2017), no. 1 011002.

[47] S. Sarkar, M. E. H. Bahri, and A. Košmrlj, *Statistical mechanics of nanotubes*, *arXiv preprint arXiv:2305.14602* (2023).

[48] M. J. Bowick, A. Košmrlj, D. R. Nelson, and R. Sknepnek, *Non-hookean statistical mechanics of clamped graphene ribbons*, *Physical Review B* **95** (2017), no. 10 104109.

[49] D. Wan, D. R. Nelson, and M. J. Bowick, *Thermal stiffening of clamped elastic ribbons*, *Physical Review B* **96** (2017), no. 1 014106.

[50] P. Z. Hanakata, S. S. Bhabesh, M. J. Bowick, D. R. Nelson, and D. Yllanes, *Thermal buckling and symmetry breaking in thin ribbons under compression*, *Extreme Mechanics Letters* **44** (2021) 101270.

[51] A. Morshedifard, M. Ruiz-García, M. J. A. Qomi, and A. Košmrlj, *Buckling of thermalized elastic sheets*, *Journal of the Mechanics and Physics of Solids* **149** (2021) 104296.

[52] S. Shankar and D. R. Nelson, *Thermalized buckling of isotropically compressed thin sheets*, *Physical Review E* **104** (2021), no. 5 054141.

[53] P. Le Doussal and L. Radzihovsky, *Thermal buckling transition of crystalline membranes*, *arXiv e-prints* (2021) arXiv–2102.

[54] T. Banerjee, N. Sarkar, J. Toner, and A. Basu, *Rolled up or crumpled: phases of asymmetric tethered membranes*, *Physical Review Letters* **122** (2019), no. 21 218002.

[55] H. S. Seung and D. R. Nelson, *Defects in flexible membranes with crystalline order*, *Physical Review A* **38** (1988), no. 2 1005.

[56] J. Lidmar, L. Mirny, and D. R. Nelson, *Virus shapes and buckling transitions in spherical shells*, *Physical Review E* **68** (2003), no. 5 051910.

[57] B. Schmidt and F. Fraternali, *Universal formulae for the limiting elastic energy of membrane networks*, *Journal of the Mechanics and Physics of Solids* **60** (2012), no. 1 172–180.

[58] R. Nicklow, N. Wakabayashi, and H. Smith, *Lattice dynamics of pyrolytic graphite*, *Physical Review B* **5** (1972), no. 12 4951.

[59] J. A. Anderson, J. Glaser, and S. C. Glotzer, *Hoomd-blue: A python package for high-performance molecular dynamics and hard particle monte carlo simulations*, *Comput. Mater. Sci.* **173** (2020) 109363.

[60] J. Glaser, T. D. Nguyen, J. A. Anderson, P. Lui, F. Spiga, J. A. Millan, D. C. Morse, and S. C. Glotzer, *Strong scaling of general-purpose molecular dynamics simulations on gpus*, *Computer Physics Communications* **192** (2015) 97–107.

[61] S. Plimpton, *Fast parallel algorithms for short-range molecular dynamics*, *Journal of computational physics* **117** (1995), no. 1 1–19.

[62] W. Humphrey, A. Dalke, and K. Schulten, *Vmd: visual molecular dynamics*, *Journal of molecular graphics* **14** (1996), no. 1 33–38.

[63] J. E. Stone, *An efficient library for parallel ray tracing and animation*, .

[64] N. Friedl, F. G. Rammerstorfer, and F. D. Fischer, *Buckling of stretched strips*, *Computers & structures* **78** (2000), no. 1-3 185–190.

[65] E. Cerda and L. Mahadevan, *Geometry and physics of wrinkling*, *Physical review letters* **90** (2003), no. 7 074302.

[66] M. Xin and B. Davidovitch, *Stretching hookean ribbons part i: relative edge extension underlies transverse compression and buckling instability*, *The European Physical Journal E* **44** (2021) 1–14.

[67] E. Guitter, F. David, S. Leibler, and L. Peliti, *Thermodynamical behavior of polymerized membranes*, *Journal de Physique* **50** (1989), no. 14 1787–1819.

[68] M. J. Bowick, S. M. Catterall, M. Falcioni, G. Thorleifsson, and K. N. Anagnostopoulos, *The flat phase of crystalline membranes*, *Journal de Physique I* **6** (1996), no. 10 1321–1345.

[69] A. Logg, K.-A. Mardal, and G. Wells, *Automated Solution of Differential Equations by the Finite Element Method: The FEniCS Book*. Springer Publishing Company, Incorporated, 2012.

[70] D. Zhou and J. Zhang, *Non-hermitian topological metamaterials with odd elasticity*, *Physical Review Research* **2** (2020), no. 2 023173.

[71] C. Scheibner, W. T. Irvine, and V. Vitelli, *Non-hermitian band topology and skin modes in active elastic media*, *Physical Review Letters* **125** (2020), no. 11 118001.

[72] Y. Chen, X. Li, C. Scheibner, V. Vitelli, and G. Huang, *Realization of active metamaterials with odd micropolar elasticity*, *Nature communications* **12** (2021), no. 1 5935.

[73] E. S. Bililign, F. Balboa Usabiaga, Y. A. Ganan, A. Poncet, V. Soni, S. Magkiriadou, M. J. Shelley, D. Bartolo, and W. T. Irvine, *Motile dislocations knead odd crystals into whorls*, *Nature Physics* **18** (2022), no. 2 212–218.

[74] A. P. Petroff, X.-L. Wu, and A. Libchaber, *Fast-moving bacteria self-organize into active two-dimensional crystals of rotating cells*, *Physical review letters* **114** (2015), no. 15 158102.

[75] T. H. Tan, A. Mietke, J. Li, Y. Chen, H. Higinbotham, P. J. Foster, S. Gokhale, J. Dunkel, and N. Fakhri, *Odd dynamics of living chiral crystals*, *Nature* **607** (2022), no. 7918 287–293.

[76] M. Shaat and H. S. Park, *Chiral nonreciprocal elasticity and mechanical activity*, *Journal of the Mechanics and Physics of Solids* **171** (2023) 105163.

[77] R. Elliott, J. Krumhansl, and P. Leath, *The theory and properties of randomly disordered crystals and related physical systems*, *Reviews of modern physics* **46** (1974), no. 3 465.

[78] S. Feng, M. Thorpe, and E. Garboczi, *Effective-medium theory of percolation on central-force elastic networks*, *Physical Review B* **31** (1985), no. 1 276.

[79] X. Mao, O. Stenull, and T. C. Lubensky, *Effective-medium theory of a filamentous triangular lattice*, *Physical Review E* **87** (2013), no. 4 042601.

[80] P. Soven, *Contribution to the theory of disordered alloys*, *Physical Review* **178** (1969), no. 3 1136.

[81] D. B. Liarte, X. Mao, O. Stenull, and T. Lubensky, *Jamming as a multicritical point*, *Physical Review Letters* **122** (2019), no. 12 128006.

[82] M. Shimada and E. De Giuli, *Random quench predicts universal properties of amorphous solids*, *SciPost Physics* **12** (2022), no. 3 090.

[83] I. Goldhirsch, *Stress, stress asymmetry and couple stress: from discrete particles to continuous fields*, *Granular Matter* **12** (2010), no. 3 239–252.

[84] J. N. Nampoothiri, Y. Wang, K. Ramola, J. Zhang, S. Bhattacharjee, and B. Chakraborty, *Emergent elasticity in amorphous solids*, *Physical review letters* **125** (2020), no. 11 118002.

[85] D. B. Liarte, O. Stenull, X. Mao, and T. Lubensky, *Elasticity of randomly diluted honeycomb and diamond lattices with bending forces*, *Journal of Physics: Condensed Matter* **28** (2016), no. 16 165402.

[86] J. C. Maxwell, *L. on the calculation of the equilibrium and stiffness of frames*, *The London, Edinburgh, and Dublin Philosophical Magazine and Journal of Science* **27** (1864), no. 182 294–299.

[87] B. DiDonna and T. Lubensky, *Nonaffine correlations in random elastic media*, *Physical Review E* **72** (2005), no. 6 066619.

[88] B. Audoly and Y. Pomeau, *Elasticity and geometry*, in *Peyresq Lectures on Nonlinear Phenomena*, pp. 1–35. World Scientific, 2000.

[89] P. M. Chaikin and T. C. Lubensky, *Principles of condensed matter physics*. Cambridge university press Cambridge, 1995.